

Chapter 3

Compact heat exchangers

3.1 Relevance of mini/micro channel compact heat exchangers

In the previous chapter, it has been pointed out that the thermal rejection process due to gascooler plays a fundamental role in determining the performances of the carbon dioxide transcritical cycle. As it is evident in the numerical simulations comparing different architectures (see Fig. 2.19) for the experimental test rig previously discussed, the efficiency of the compact heat exchanger dedicated to heat rejection affects the cooling capacity more than the evaporator itself, at least for the considered operating conditions. Moreover, the possibility of using again carbon dioxide as working fluid in the refrigerating plants with performances which try to approach those of usual devices based on synthetic fluids, mainly relies upon a miniaturization process. Miniaturization enables to improve the efficiency of the components concerning heat transfer and consequently to reduce the gap between carbon dioxide and synthetic fluids. In particular, this deals with the design of mini/micro channel compact heat exchangers. In this chapter, mini/micro channel compact heat exchangers will be investigated in order to analyze the effects due to undesired conduction, which is considered one of the reasons limiting their widespread diffusion in refrigeration technology.

Finned heat exchangers made of flat extruded aluminum tubes with internal mini/micro channels are a topical subject, which is becoming very important in refrigeration technology. With respect to the traditional finned coil heat exchangers, they appear to have a better energy efficiency, in terms of larger heat transfer capability with the same mechanical power spent for circulation of the working fluids. This is true for both fluid sides of the heat exchanger. Furthermore, mini/micro channel tubes, because of their high mechanical resistance to the internal pressure, are a suitable solution for gas cooling in carbon dioxide transcritical cycles. The optimization of this type of heat exchanger is therefore one of the main research goal for the development of refrigerating systems operated with this natural fluid. High gascooler thermal efficiency is an essential condition to obtain high COP values, since a low value of the carbon dioxide temperature at its outlet increases the cooling capacity, thus allowing a reduction of the highest pressure and the mechanical compression power. In fact, the optimal upper pressure value can be regarded, at a rough estimate, as inversely proportional to the gascooler thermal efficiency [42].

The gascooler analysis, aimed at optimizing its design, faces the problem related to the wide variations of thermodynamical and thermophysical properties near the critical point: using a high-resolution mesh is the mandatory solution. This can be very expensive in terms of computational resources. In the following, a numerical technique is proposed ¹ in order to partially mitigate this problem.

¹Part of the contents discussed in this chapter was previously published in two papers:

- P. Asinari, “Finite-volume and Finite-element Hybrid Technique for the Calculation of Complex Heat Exchangers by Semiexplicit Method for Wall Temperature Linked Equations (SEW-TLE)”, *Numerical Heat Transfer: Fundamentals*, Vol. 45, pp. 221-247 (2004);
- P. Asinari, L. Cecchinato, E. Fornasieri, “Effects of Thermal Conduction in Microchannel Gas Coolers for Carbon Dioxide”, *International Journal of Refrigeration*, Vol. 27, pp. 577-586 (2004).

3.2 Modeling of compact heat exchangers

3.2.1 General framework

The first theoretical efforts on compact heat exchangers modeling produced analytical treatment of idealized devices. These works produced a range of global methods, like the Logarithmic Mean Temperature Difference (LMTD) and the Effectiveness - Number of Transfer Units (ϵ -NTU) [43]. However, global methods are based on a number of assumptions (i.e. steady flow, single-phase flow, constant thermo-physical properties, constant heat transfer coefficients, negligible longitudinal wall conduction and so on), which are hardly met in practical applications. In particular, real heat exchangers often involve two-phase flow processes, air dehumidification and variable fluid properties.

In addition, the interest for more sophisticated heat exchangers is increasing because of the need for better overall efficiency and decrease in size and weight. In all varieties of powered vehicles from automobiles to spacecrafts, the trend for small-size and lightweight heat exchangers has stimulated the development of much more compact heat transfer surfaces than in classical devices [44]. In compact devices, some effects neglected by classical theory can influence the overall behavior. Obviously, a rationally optimized heat exchanger design and the definition of new surfaces with better characteristics require the development of reliable simulation tools.

The need for detailed analysis of practical situations demands the employment of computational techniques, which realize a close representation of reality. Nowadays, a lot of general-purpose codes for Computational Fluid Dynamics (CFD) are available and can be applied to heat exchangers. Despite its versatility, a general-purpose code can be characterized by some drawbacks if compared with an application-oriented

one. In particular, a general purpose code can require large meshes and unacceptable computational time to describe specific details of complex applications. Furthermore, some parametric studies involve geometric characteristics, which need frequent re-meshing and heavy post-processing. Finally, general-purpose codes are not usually suitable to produce a stand-alone module for the coupled analysis concerning both the heat exchanger and the whole system in which it is installed. This goal can only be achieved by iteratively modifying the boundary conditions of the problem.

On the other hand, application-oriented codes for modeling heat exchangers apply discretization techniques which, although general in nature, have been fitted to the analysis of a particular effect. Some examples can be found in literature which consider longitudinal heat conduction [45, 46], non-uniformity of the inlet fluid flow [47] or the mutual interaction between the previous effects [48, 49].

Only a few studies have been devoted to discussing and developing a general numerical formulation. Recently, a general numerical approach for compact heat exchangers, called SemiExplicit method for Wall Temperature Linked Equations SEWTLE, has been proposed [50]. The method decouples the calculation of wall and fluid temperature fields and computes the final solution by means of an iterative procedure which is controlled by heat flow continuity between hot-side and cold-side thermal flux. Since this method uses thermal balance as convergence check, an intrinsically conservative scheme for the discretization of involved equations, as the Finite Volume Method (FVM), represents the most natural choice and it was included in the original paper.

For modeling mini/micro channel compact heat exchangers, the SEWTLE technique seems promising but the FVM requires too large meshes because of wall discretization, if the finned surfaces are fully taken into account. In the following,

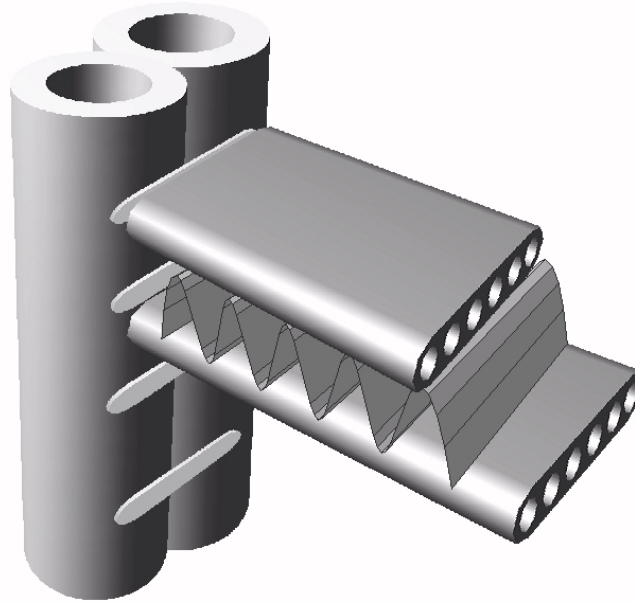


Figure 3.1: Typical mini/micro channel compact heat exchanger for carbon dioxide cooling (courtesy of SINTEF).

the SEWTLE technique will be generalized in order to include different numerical schemes, which allow us to reduce the computational demand.

3.2.2 Problem definition

A typical example of mini/micro channel compact heat exchanger for carbon dioxide cooling is shown in Fig. 3.1. As a first approximation, it is possible to simplify the round shape section of the mini/micro channels and to consider instead a rectangular section with an effective perimeter, which realizes the same heat transfer surface. The heat transfer coefficients may be corrected too by means of proper geometrical factors. This assumption allows us to highly simplify the topology of the problem and it does not substantially modify the reliability of the results, as it will be shown when the numerical results will be compared with the experimental data.

Generally, the equations describing a heat exchanger are defined on a computa-

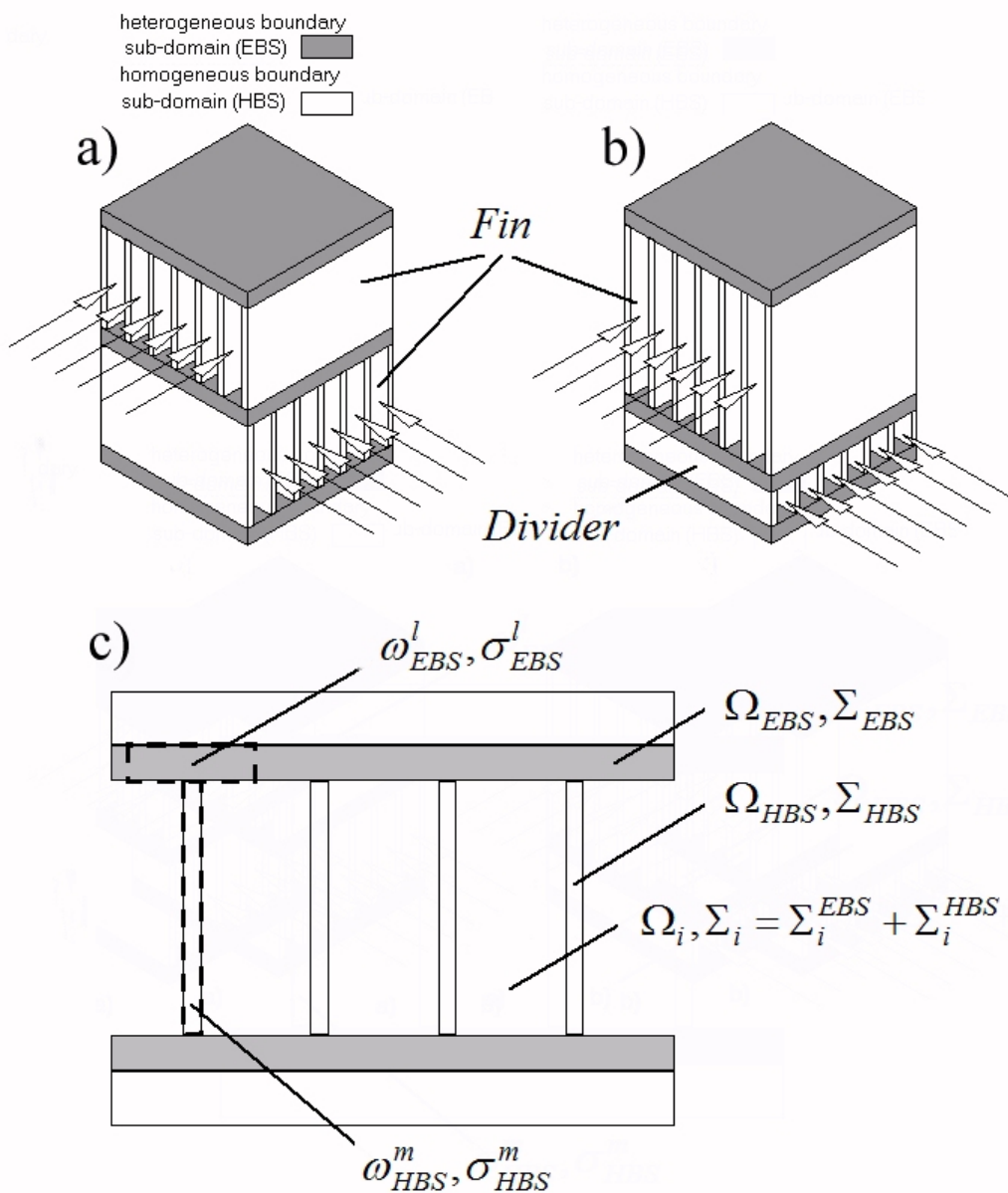


Figure 3.2: Visualization of conventional nomenclature: difference between heterogeneous boundary subdomain (EBS) and homogeneous boundary subdomain (HBS), between fins and dividers and between global calculation domain Ω and discretized domains ω . (a) Crossflow plate-fin heat exchanger. (b) Crossflow plate-fin heat exchanger with mini/micro channels. (c) Considered discretization.

tional domain composed by the fluid region and the surrounding wall. The fluid region can be divided into a set of one-dimensional streams, following the flow direction. The possibility of a mixing region, which receives some fluid streams and produces average conditions, can be easily included. In this case, the FVM represents the easiest choice for the discretization of fluid equations.

On the other hand, the situation is not so easy for the wall domain. In fact, a distinction always exists among the separating walls which constitute the heat exchanger: some of them are in direct contact with fluids of different nature, while some others are in contact with fluids of the same nature. Referring to phenomenon of convection, the first class of separating walls constitutes the heterogeneous boundary sub-domain (EBS), while the last class constitutes the homogeneous boundary sub-domain (HBS): for instance, the case of crossflow plate-fin heat exchanger is reported in Fig. 3.2*a*. The EBS is the physical substratum which makes heat transfer possible between different fluids (hot-side and cold-side) while the HBS is an optional extension of separating wall, which has been introduced for enhancing heat transfer surfaces. For crossflow plate-fin heat exchangers, the EBS is constituted by the surfaces due to the span of both fluid directions while the HBS couples the previous surfaces by transverse fins. Finally, the EBS is usually characterized by convective fluxes due to strong temperature gradients while the HBS involves small inhomogeneities of temperature field due to adjacent fluid streams. Since the numerical discretization must match the physical behavior of the considered portion, the distinction between EBS and HBS suggests choosing different schemes, if the above discrepancies are relevant.

The difference between the discussed sub-domains becomes evident when a low heat transfer coefficient characterizes one of the fluids. For the mini/micro channel

heat exchangers for carbon dioxide cooling, the air fins allow us to increase the heat transfer surface, while the separating walls in the generic flat tube simply allow us to identify the mini/micro channels (see Fig. 3.2*b*). In this case, the fin surface is mainly responsible for the whole device performance. When one of the fin roots is characterized by inverse thermal flux directed toward the heated wall, the fin efficiency is drastically reduced and a thermal short circuit exists. The importance of thermal short circuit has been shown analytically in simplified configurations [51] and by means of detailed simulations for a particular fin surface [52]. Unfortunately, thermal short circuit is influenced by the topology of fluid streams because they contribute to determine the final temperature distribution. Detailed simulations for whole HBS are not practical in many cases and, moreover, a reduction of unknown variables must be performed in order to simplify the calculations while preserving the physical meaning.

3.3 Physical model formulation

3.3.1 Governing equations

Let us consider again the compact heat exchanger shown in Fig. 3.2*b*. The following considerations can be easily extended to different flow arrangements and geometry. With the purpose to identify the sub-domains which constitute the calculation domain Ω_c , some definitions are introduced for volumes, as shown in Fig. 3.2*c*:

$$\begin{aligned}
 \Omega_w &\doteq \Omega_{EBS} \cup \Omega_{HBS}, \\
 \Omega_f &\doteq \bigcup_{i=1}^{N_{fs}} \Omega_i, \\
 \Omega_c &\doteq \Omega_w \cup \Omega_f,
 \end{aligned} \tag{3.1}$$

where Ω_w is the wall domain, which can be divided in Ω_{EBS} for heterogeneous bound-

ary subdomain (EBS) and Ω_{HBS} for homogeneous boundary subdomain (HBS), while Ω_f is the fluid domain, which can be divided into N_{fs} sub-domains Ω_i for each fluid. Additional definitions are introduced for surfaces, as shown again in Fig. 3.2c:

$$\begin{aligned}\Sigma_f &\doteq \bigcup_{i=1}^{N_{fs}} \Sigma_i, \\ \Sigma_w &\doteq \Sigma_{EN} \cup \Sigma_f, \\ \Sigma_i &\doteq \Sigma_i^{EBS} \cup \Sigma_i^{HBS},\end{aligned}\tag{3.2}$$

where Σ_{EN} is the portion of wall surface which is in contact with the external environment.

For steady conditions and single-phase flow, the energy conservation equations can be written for each sub-domain, namely:

$$P \in \Omega_i \quad \int_{\Sigma_i} \rho_i h_i \mathbf{u}_i \cdot \mathbf{n} dA = \int_{\Sigma_i} \mathbf{J}_i \cdot \mathbf{n} dA + \int_{\Omega_i} S_i dV,\tag{3.3}$$

$$P \in \Omega_w \quad \int_{\Omega_w} \nabla_3 \cdot (\lambda_w \nabla_3 T_w) dV = - \sum_{i=1}^{N_{fs}} \int_{\Sigma_i} \mathbf{J}_i \cdot \mathbf{n} dA - \int_{\Sigma_{EN}} \mathbf{J}_{EN} \cdot \mathbf{n} dA = 0,\tag{3.4}$$

where

$$\mathbf{J}_i \doteq - \lambda_i \nabla_3 T_i,$$

and N_{fs} is the number of fluid streams in the heat exchanger. The vector \mathbf{n} is perpendicular to Σ_i and directed outwards of the domain. Since no energy generation has been supposed inside the wall, the overall thermal balance involves only fluid streams, which yields:

$$\sum_{i=1}^{N_{fs}} \left(\int_{\Sigma_i} \rho_i h_i \mathbf{u}_i \cdot \mathbf{n} dA - \int_{\Omega_i} S_i dV \right) + \int_{\Sigma_{EN}} \mathbf{J}_{EN} \cdot \mathbf{n} dA = 0.\tag{3.5}$$

In addition to the energy conservation equation, the momentum conservation and the continuity equations should be considered to provide the full system of Navier-Stokes equations needed to calculate pressure and velocity. However, some simplifying

hypotheses can be introduced. If the fluid is incompressible, the fluid streams have constant section and the viscosity is constant, the energy equation can be decoupled from the system and solved independently. If the fluid flow is assumed one-dimensional, it is not possible to calculate the cross flow gradients involved in convective fluxes, which must be calculated by means of heat transfer phenomenological coefficients. Finally, if the viscous dissipation can be neglected, the heat generation in the energy conservation equations can be removed. These simplifying assumptions can be applied to the previous energy equations:

$$P \in \Omega_i \quad \int_{A_U+A_D} \rho_i h_i \mathbf{u}_i \cdot \mathbf{n} dA = \int_{\Sigma_i} \mathbf{J}_i \cdot \mathbf{n} dA, \quad (3.6)$$

where

$$\mathbf{J}_i \doteq \alpha_i (T_w - T_i) \mathbf{n},$$

and α_i is the convective phenomenological coefficient. Before proceeding to discretization of the previous equations, the boundary conditions will be discussed.

3.3.2 Boundary conditions

Usually at the fluid inlet, Dirichlet-type conditions are imposed because the fluid states depend on the behavior of the upstream devices. On the other hand, a Neumann-type condition is imposed on the portion of the wall surface which is in contact with the external environment, because the heat exchangers are usually well insulated. These boundary conditions can be summarized as:

$$\forall i : 1 \leq i \leq N_{fs} \quad T_i^U = \text{cost} \quad ; \quad \int_{\Sigma_{EN}} \mathbf{J}_{EN} \cdot \mathbf{n} dA = 0. \quad (3.7)$$

The resulting system of equations is composed by a sub-system of ordinary differential equations (ODEs), one for each fluid stream, with Dirichlet-type boundary conditions

and a partial differential equation (PDE) for the separating wall with Neumann-type boundary condition. When the longitudinal conduction is negligible and the convective heat transfer coefficients do not depend on the wall temperature, the PDE becomes a linear condition for wall temperature which can be expressed as function of the neighboring fluid temperatures. In this way, the system can be reduced to a pure system of ODEs.

Unfortunately, in order to investigate the effects due to thermal short circuit, the last hypothesis does not hold and it is useful to include the calculation of wall temperature in the numerical procedure [50]. Since this calculation is time-consuming, we need to choose properly the cell discretization and the numerical scheme for the wall.

3.4 Numerical implementation

The mesh construction can be divided in two steps. The first step replaces the continuous information contained in the exact solution of differential equations with discrete values at a finite number of locations in the calculation domain (*grid* points). Obviously, the best grid choice depends on the nature of the differential equations. For this reason, in Fig. 3.3, the grid points for the wall domain governed by PDE (square markers) have been separated from the grid points for a generic fluid sub-domain governed by ODE (arrow markers). For the accuracy of the numerical results, the relative arrangement between wall and fluid grid must be discussed. Three cases are considered: longitudinal configuration (see Fig. 3.3*a*); transverse configuration (see Fig. 3.3*b*) and diagonal configuration (see Fig. 3.3*c*). The longitudinal configuration shows an important drawback because the wall temperature at the intersection between the general portion for EBS and the corresponding one for HBS is not directly

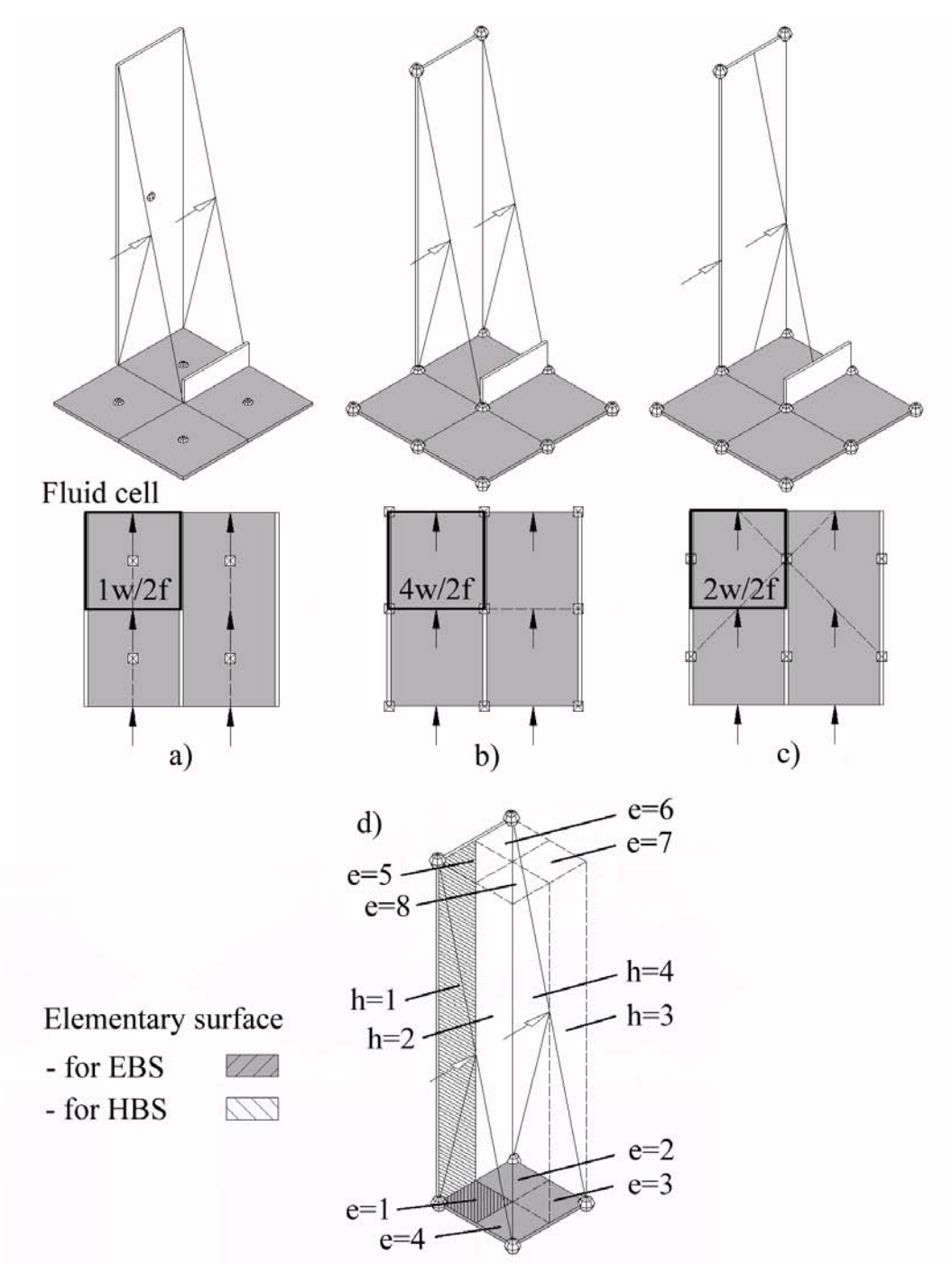


Figure 3.3: Relative arrangement between wall grid (square markers) and fluid grid (arrow markers): (a) longitudinal configuration; (b) transverse configuration and (c) diagonal configuration. All configurations show the projection of fluid cell adopted in calculations and the ratio between wall points and fluid ones (w/f). (d) Numeration of elementary surfaces for fluid cell with transverse configuration.

considered and must be evaluated by interpolation. In practical applications, this means that the longitudinal configuration is not suitable for studying the behavior of fins because it does not consider the fin root temperatures. Between two consecutive fluid grid points (arrow markers), the temperature profile inside the portion of heat transfer surface must be approximated by means of wall grid points (square markers). If we compare the ratios between wall points and fluid ones within a projection of generic fluid cell (see Figs. 3.3*a*, 3.3*b* and 3.3*c*), we find that the longitudinal configuration is the most penalized ($1w/2f$), followed by the diagonal one ($2w/2f$), while the transverse configuration is the most convenient ($4w/2f$). Although the decoupling between fluid and wall conditions increases the computational time, the transverse configuration will be adopted in the following.

The second step of the mesh definition is constituted by *cell* discretization, i.e. the subdivision of the calculation domain in suitable computational cells. Since each numerical scheme is characterized by preferable distribution of the grid points within the elementary control volume, the cell discretization arises from the choice of the numerical scheme. The discussion about this choice has been split among the different parts of the calculation domain, as to demonstrate that the utilization of different numerical schemes is possible within the framework of the same grid configuration.

3.4.1 Discretized equations for fluid domain

The fluid streams are governed by ODEs characterized by first-order spatial derivative as main term. In this case, the Finite Volume Method (FVM) is the most natural choice and the use of a grid point at the fluid inlet and another one at the fluid outlet of the control volume is recommended. In this way, the first derivative can be efficiently approximated by the corresponding finite-difference expression linking the

well-defined values of the variable at both ends [53].

If the fluid grid points are located at the control volume edges, the number of fluid cells N_i and their distribution are strictly tied to the grid spatial density. Inside each control volume, a distinction can be made between the surfaces belonging to different sub-domains (EBS or HBS). Let us introduce the definitions for discretized surfaces, namely:

$$\Sigma_i \doteq \bigcup_{j=1}^{N_i} \Delta\Sigma_{i,j}. \quad (3.8)$$

Applying an up-wind technique, Eq. (3.6) produces N_f algebraic conditions for the fluid domain. This yields:

$$\begin{aligned} \forall i, j \quad &: \quad 1 \leq i \leq N_{fs}, \quad ; \quad 1 \leq j \leq N_i, \\ G_i c_p (T_i^j - T_i^{j-1}) &= \int_{\Delta\Sigma_{i,j}^{EBS}} \mathbf{J}_{i,j} \cdot \mathbf{n} dA + \int_{\Delta\Sigma_{i,j}^{HBS}} \mathbf{J}_{i,j} \cdot \mathbf{n} dA, \end{aligned} \quad (3.9)$$

where

$$\forall i : 1 \leq i \leq N_{fs} \quad ; \quad T_i^0 = T_i^U = \text{cost} \quad ; \quad N_f = \sum_{i=1}^{N_{fs}} N_i.$$

The previous integrals are expressed as the sum of a finite number of terms, which represent the convective thermal fluxes exchanged through elementary surfaces. For clarifying this subdivision, two elementary surfaces are shown in Fig. 3.3*d*, one for each wall sub-domain. Within each fluid cell, the identification of an elementary surface can be done by a local index which depends on the considered wall sub-domain (e for EBS and h for HBS), namely:

$$\begin{aligned} \Delta\Sigma_{i,j}^{EBS} &\doteq \bigcup_{e=1}^8 \Delta\Sigma_{i,j,e}^{EBS}, \\ \Delta\Sigma_{i,j}^{HBS} &\doteq \bigcup_{h=1}^4 \Delta\Sigma_{i,j,h}^{HBS}. \end{aligned} \quad (3.10)$$

In this way, the discretized fluid equations reduce to the following form:

$$\begin{aligned} \forall i, j: 1 \leq i \leq N_{fs}, \quad ; \quad 1 \leq j \leq N_i, \\ G_i c_p (T_i^j - T_i^{j-1}) = \sum_{e=1}^8 \Delta \Phi_{i,j,e}^{EBS} + \sum_{h=1}^4 \Delta \Phi_{i,j,h}^{HBS}, \end{aligned} \quad (3.11)$$

where

$$\Delta \Phi_{i,j,e}^{EBS} \doteq \int_{\Delta \Sigma_{i,j,e}^{EBS}} \mathbf{J}_{i,j} \cdot \mathbf{n} dA, \quad (3.12)$$

$$\Delta \Phi_{i,j,h}^{HBS} \doteq \int_{\Delta \Sigma_{i,j,h}^{HBS}} \mathbf{J}_{i,j} \cdot \mathbf{n} dA. \quad (3.13)$$

These equations involve the calculation of thermal fluxes which must be consistent with the profile assumptions for both fluid and wall.

3.4.2 Discretized equations for heterogeneous wall sub-domain

Since the wall domain has been subdivided into two sub-domains, a suitable repartition technique must be adopted. Consistent with the purpose of reducing the computational effort for HBS, all the wall grid points are supposed as belonging to EBS. In this way, in the resulting algebraic system there will be no equation which explicitly prescribes the energy conservation for HBS. The last condition will be considered implicitly when deriving the thermal flux expressions.

The governing equations for wall sub-domains can be derived, such as to express the effect of thermal coupling. Equation (3.4) can be split into two equations, one for each sub-domain:

$$P \in \Omega_{EBS} \quad ; \quad \int_{\Omega_{EBS}} \nabla_3 \cdot (\lambda_w \nabla_3 T_w) dV = - \sum_{i=1}^{N_{fs}} \int_{\Sigma_{EBS}} \mathbf{J}_i \cdot \mathbf{n} dA + \Phi_{XBS} = 0, \quad (3.14)$$

$$P \in \Omega_{HBS} \quad ; \quad \int_{\Omega_{HBS}} \nabla_3 \cdot (\lambda_w \nabla_3 T_w) dV = - \sum_{i=1}^{N_{fs}} \int_{\Sigma_{HBS}} \mathbf{J}_i \cdot \mathbf{n} dA - \Phi_{XBS} = 0, \quad (3.15)$$

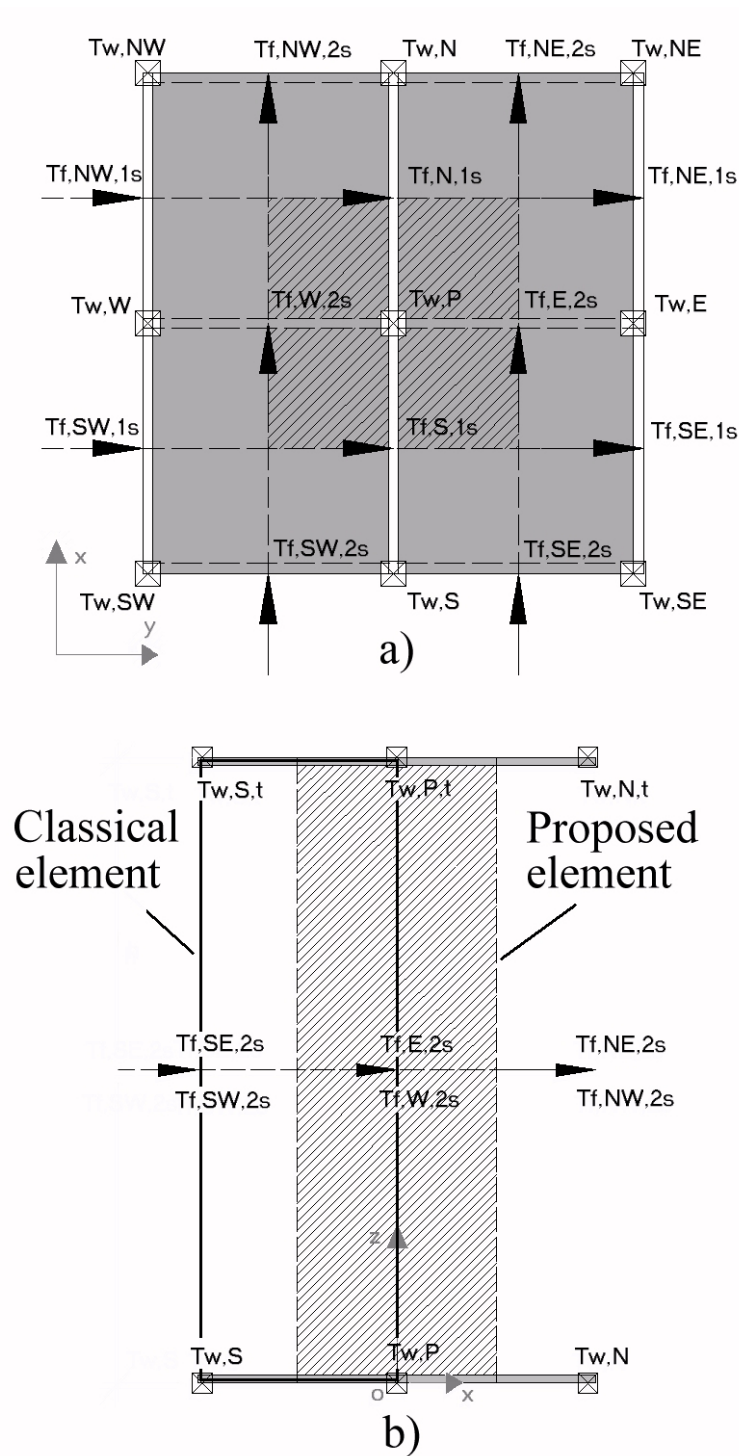


Figure 3.4: Schematic view of the EBS cell (a) and HBS cell (b) surrounded by fluid paths involved in the convective heat transfer. In the HBS cell, the comparison between the proposed element and classical one is also reported.

where

$$\Phi_{XBS} = - \int_{\Sigma_{EBS} \cap \Sigma_{HBS}} \lambda_w \nabla_3 T_w \cdot \mathbf{n}_w dA,$$

is the relation used to enforce thermal flux balance between HBS and EBS. The vector \mathbf{n}_w must be considered oriented towards a direction leaving from HBS and, consequently, entering into EBS. The first equation will be employed to determine the discretization conditions for wall grid points, while the last one will be involved in the definition of flux Φ_{XBS} exchanged between HBS and EBS.

Also in this case the FVM is recommended. A central control volume with a value of temperature defined at its centroid is adopted because it represents the most suitable configuration to evaluate second-order partial spatial derivatives. With the transverse grid configuration, some care must be taken to define half-volumes at the edge of the plates, such as to properly satisfy the boundary conditions [53]. The ambiguity due to the definition of wall temperatures at the fluid grid locations can be easily overcome by interpolation among the available values in EBS.

If the wall grid point is located at the control volume center, the cell discretization is completely defined (Fig. 3.4a). The EBS can be subdivided into N_{EBS} control volumes, namely:

$$\Omega_{EBS} = \sum_{l=1}^{N_{EBS}} \omega_l^{EBS}. \quad (3.16)$$

Taking into account this discretization and introducing the fin thickness s , Eq. (3.14) produces N_{EBS} algebraic conditions for the wall:

$$\begin{aligned} \forall l \quad &: \quad 1 \leq l \leq N_{EBS}, \\ \int_{\sigma_{EBS}^l} \nabla_2 \cdot (\lambda_w \nabla_2 T_w) s dA &= \Delta \Phi_l^{EBS} - \Delta \Phi_l^{XBS}, \end{aligned} \quad (3.17)$$

where

$$\Delta \Phi_l^{EBS} = \sum_{i=1}^{N_{fs}} \int_{\sigma_{EBS}^l} \mathbf{J}_i \cdot \mathbf{n} dA,$$

$$\Delta\Phi_l^{XBS} = - \int_{\sigma_l^{EBS} \cap \Sigma_{HBS}} \lambda_w \frac{\partial T_w}{\partial z} \mathbf{n}_z \cdot \mathbf{n}_w dA,$$

and \mathbf{n}_z is the unit vector of z -axis. Recalling the definitions expressed by Eqs. (3.12) and considering separately the contribution of each elementary surface to the exchanged flux $\Delta\Phi_l^{XBS}$, the discretized equations for the wall reduce to the following form:

$$\forall l : 1 \leq l \leq N_{EBS},$$

$$\int_{\sigma_l^{EBS}} \nabla_2 \cdot (\lambda_w \nabla_2 T_w) s dA = \sum_{(i,j,e) \in \mathcal{Z}_l^{EBS}} (\Delta\Phi_{i,j,e}^{EBS} - \Delta\Phi_{i,j,e}^{XBS}), \quad (3.18)$$

where

$$\mathcal{Z}_l^{EBS} = \{\forall(i, j, e) : \Delta\Sigma_{i,j,e}^{EBS} \subset \sigma_l^{EBS}\}.$$

The congruence between the wall-side and the fluid-side heat transfer calculations can be easily verified, taking into account the following equivalence:

$$\sum_{l=1}^{N_{EBS}} \sum_{(i,j,e) \in \mathcal{Z}_l^{EBS}} \Delta\Phi_{i,j,e}^{EBS} = \sum_{i=1}^{N_{fs}} \sum_{j=1}^{N_i} \sum_{e=1}^8 \Delta\Phi_{i,j,e}^{EBS}. \quad (3.19)$$

In the next section, the discretization of the wall domain will be completed.

3.4.3 Discretized equations for the homogeneous wall subdomain

Although the governing equation is the same one previously considered for EBS, the choice of the numerical approach must guarantee a physically meaningful description by using only fin root temperatures. Within the set of integral formulations, two possibilities are suitable to discretize the governing equations for HBS: *subdomain approach*, which is the basis of FVM, and *variational approach*, which is the basis of the Finite Element Method (FEM) for problems which do not involve first-derivative terms [54].

The subdomain approach is a particular case of a weighted residual formulation, where each weighting function is selected as unit over a specific portion of the calculation domain. Since the integral form of the energy conservation equation can be expressed in terms of thermal fluxes, the FVM applied to conduction problems must ensure the continuity of first-order partial spatial derivative at the border of adjacent volumes. A central control volume with a value of temperature defined at its centroid represents the easiest way to reach this goal.

The variational approach involves a functional which must be minimized over each discretization element according to the calculus of variations. The FEM considers trial temperature profiles which are continuous piecewise smooth functions and identifies among them the approximate solution which gives the minimum value of the functional. A surrounded element with temperature values defined at the border represents the easiest choice.

In our case, the discretization cell for the generic fin should be characterized by coherent description of thermal fluxes due to longitudinal conduction and by detailed temperature profile in transverse direction. As it will be clearer in the following, it is suitable to locate the temperature values at the middle of root edges, as shown in Fig. 3.4*b*. The HBS can be divided into N_{HBS} elements:

$$\Omega_{HBS} = \sum_{m=1}^{N_{HBS}} \omega_m^{HBS}. \quad (3.20)$$

Taking into account this discretization and recalling the definitions for thermal fluxes due to convection, Eq. (3.15) can be modified:

$$\forall m : 1 \leq m \leq N_{HBS}, \quad \int_{\sigma_m^{HBS}} \left[s \nabla_2 \cdot (\lambda_w \nabla_2 T_w) - \sum_{i=1}^{N_{fs}} \alpha_i (T_w - T_i) \right] dA = 0. \quad (3.21)$$

Assuming the thermal conductivity as temperature invariant, the resolution of the

previous equation can be considered equivalent to the minimization of the following functional:

$$\Pi = \int_{\sigma_m^{HBS}} \left[(\nabla_2 T_w) \cdot (\nabla_2 T_w) + \sum_{i=1}^{N_{fs}} \frac{\alpha_i}{\lambda_w s} (T_w - T_i)^2 \right] dA. \quad (3.22)$$

Let us apply the Euler-Ostrogradskij equation [55], which yields:

$$P \in \sigma_m^{HBS} \quad \frac{\partial^2 \theta}{\partial x^2} + \frac{\partial^2 \theta}{\partial z^2} = \frac{Bi}{z_0^2} \theta, \quad (3.23)$$

where

$$Bi = z_0^2 \frac{\sum_{i=1}^{N_{fs}} \alpha_i}{\lambda_w s} \quad ; \quad \theta = T_w - \frac{\sum_{i=1}^{N_{fs}} \alpha_i T_i}{\sum_{i=1}^{N_{fs}} \alpha_i}.$$

The solution of the Euler-Ostrogradskij equation is the temperature profile which gives the minimum value of the functional given by Eq. (3.22). Assuming constant fluid temperatures for the considered element, an analytical solution can be found, according to the classical theory for extended surface heat transfer [56]. The analytical solution is:

$$\begin{aligned} \theta(x, z) = & C_1 \exp\left(\sqrt{Bi} \frac{x}{z_0}\right) + C_2 \exp\left(-\sqrt{Bi} \frac{x}{z_0}\right) + \\ & C_3 \exp\left(\sqrt{Bi} \frac{z}{z_0}\right) + C_4 \exp\left(-\sqrt{Bi} \frac{z}{z_0}\right). \end{aligned} \quad (3.24)$$

The most natural choice for HBS element is the surrounded quadratic element shown in Fig. 3.4b. This is equivalent to consider four Dirichlet conditions for determining the constants C_i . Since, unfortunately, these conditions are not linearly independent for the analytical solution given by Eq. (3.24), they do not allow us to uniquely define the set of constants. A different approach was developed by the author in order to make intrinsically conservative the numerical scheme. The basic idea is to “shift” or “move” the element, as shown in Fig. 3.4b. In this case, two boundary conditions belong to Dirichlet-type while the other two to Neumann-type. The whole set of

conditions is:

$$\begin{aligned}\theta(0, 0) &= T_{w,P} - \frac{\alpha_{E,2s}}{\alpha_{E,2s} + \alpha_{W,2s}} T_{f,E,2s} - \frac{\alpha_{W,2s}}{\alpha_{E,2s} + \alpha_{W,2s}} T_{f,W,2s}, \\ \theta(0, z_0) &= T_{w,P,t} - \frac{\alpha_{E,2s}}{\alpha_{E,2s} + \alpha_{W,2s}} T_{f,E,2s} - \frac{\alpha_{W,2s}}{\alpha_{E,2s} + \alpha_{W,2s}} T_{f,W,2s},\end{aligned}\quad (3.25)$$

$$\begin{aligned}\int_0^{z_0} \lambda_w \left[\frac{\partial \theta(x, z)}{\partial x} \right]_{x=-0.5\delta x} s dz &= \lambda_w \frac{T_{w,P,t} - T_{w,S,t} + T_{w,P} - T_{w,S}}{2\delta x} s z_0, \\ \int_0^{z_0} \lambda_w \left[\frac{\partial \theta(x, z)}{\partial x} \right]_{x=+0.5\delta x} s dz &= \lambda_w \frac{T_{w,N,t} - T_{w,P,t} + T_{w,N} - T_{w,P}}{2\delta x} s z_0,\end{aligned}\quad (3.26)$$

where δx is the width of the generic finite element. Unlike that resulting from the adoption of the surrounded element, this system of equations can be uniquely solved. The first two conditions, given by Eqs. (3.25), involve the fin root temperatures while the last ones, given by Eqs. (3.26), ensure a coherent description of thermal fluxes due to longitudinal conduction.

The proposed element makes use of different profile assumptions for calculating temperature and its derivative at the border. In this way, an additional advantage arises: since Eqs. (3.26) force both side fluxes to be equal to FVM-like expressions, the continuity of fluxes at the border is satisfied for the whole extended surface too. As it will be clear in the following with regard to the solution procedure, this feature is essential for the SEWTLE technique because small discontinuities in the thermal fluxes can prevent convergence. Fortunately, the finite-volume description of EBS and the finite-element description of HBS by means of intrinsically conservative elements can be adopted together with SEWTLE.

Finally, the determined temperature profile can be used for calculating thermal fluxes through elementary surfaces. Let us consider the generic fluid cell (i, j) shown in Fig. 3.3d and suppose that $\alpha_{E,2s} = \alpha_{W,2s} = \alpha$ and $T_{f,E,2s} = T_{f,W,2s} = T_f$. The temperature profile defined by the variational principle must be calculated first by

Eqs. (3.25, 3.26). This means solving the following system of equations:

$$\begin{cases} C_1 + C_2 + C_3 + C_4 = T_{w,P} - T_f \\ C_1 + C_2 + C_3 a + C_4/a = T_{w,P,t} - T_f \\ C_1/\sqrt{b} - C_2\sqrt{b} = z_0 (T_{w,P,t} - T_{w,S,t} + T_{w,P} - T_{w,S}) / (2\delta x \sqrt{Bi}) \\ C_1\sqrt{b} - C_2/\sqrt{b} = z_0 (T_{w,N,t} - T_{w,P,t} + T_{w,N} - T_{w,P}) / (2\delta x \sqrt{Bi}) \end{cases}, \quad (3.27)$$

where

$$a = \exp(\sqrt{Bi}) \quad ; \quad b = \exp(\sqrt{Bi} \delta x / z_0).$$

This system of equations allows us to determine the generic constants C_i and to identify the element temperature profile. The constants C_i are linear functions of unknown fluid temperatures, upstream temperatures and unknown wall temperatures.

The convective thermal fluxes for HBS elementary surfaces can be expressed as:

$$h = 2, 3 \quad \Delta\Phi_{i,j,h}^{HBS} = \int_0^{z_0} \int_{-0.5\delta x}^0 \alpha \theta(x, z) dx dz, \quad (3.28)$$

$$h = 1, 4 \quad \Delta\Phi_{i,j,h}^{HBS} = \int_0^{z_0} \int_0^{0.5\delta x} \alpha \theta(x, z) dx dz. \quad (3.29)$$

Introducing the element temperature profile, the previous integrals can be evaluated:

$$h = 2, 3 \quad \Delta\Phi_{i,j,h}^{HBS} = \alpha \frac{z_0^2}{\sqrt{Bi}} \left[(\sqrt{b} - 1) C_1 + \left(1 - \frac{1}{\sqrt{b}}\right) C_2 + \right. \quad (3.30)$$

$$\left. \frac{1}{2} \frac{\delta x}{z_0} (a - 1) C_3 + \frac{1}{2} \frac{\delta x}{z_0} \left(1 - \frac{1}{a}\right) C_4 \right], \quad (3.31)$$

$$h = 1, 4 \quad \Delta\Phi_{i,j,h}^{HBS} = \alpha \frac{z_0^2}{\sqrt{Bi}} \left[\left(1 - \frac{1}{\sqrt{b}}\right) C_1 + (\sqrt{b} - 1) C_2 + \right. \quad (3.32)$$

$$\left. \frac{1}{2} \frac{\delta x}{z_0} (a - 1) C_3 + \frac{1}{2} \frac{\delta x}{z_0} \left(1 - \frac{1}{a}\right) C_4 \right].$$

The conductive thermal fluxes for XBS elementary surfaces can be expressed in the same way, namely:

$$e = 1, 4 \quad \Delta\Phi_{i,j,e}^{XBS} = \int_0^{0.5\delta x} \frac{\lambda_w s}{2} \left[\frac{\partial \theta(x, z)}{\partial z} \right]_{z=0} dx, \quad (3.33)$$

$$e = 2, 3 \quad \Delta\Phi_{i,j,e}^{XBS} = \int_{-0.5\delta x}^0 \frac{\lambda_w s}{2} \left[\frac{\partial \theta(x, z)}{\partial z} \right]_{z=0} dx, \quad (3.34)$$

$$e = 5, 8 \quad \Delta\Phi_{i,j,e}^{XBS} = - \int_0^{0.5\delta x} \frac{\lambda_w s}{2} \left[\frac{\partial\theta(x, z)}{\partial z} \right]_{z=z_0} dx, \quad (3.35)$$

$$e = 6, 7 \quad \Delta\Phi_{i,j,e}^{XBS} = - \int_{-0.5\delta x}^0 \frac{\lambda_w s}{2} \left[\frac{\partial\theta(x, z)}{\partial z} \right]_{z=z_0} dx. \quad (3.36)$$

Introducing the element temperature profile, the previous integral can be evaluated:

$$e = 1, 2, 3, 4 \quad \Delta\Phi_{i,j,e}^{XBS} = \frac{\lambda_w s}{4} \sqrt{Bi} \frac{\delta x}{z_0} (C_3 - C_4), \quad (3.37)$$

$$e = 5, 6, 7, 8 \quad \Delta\Phi_{i,j,e}^{XBS} = \frac{\lambda_w s}{4} \sqrt{Bi} \frac{\delta x}{z_0} (a C_3 - C_4/a). \quad (3.38)$$

Since the previous fluxes, given by Eqs. (3.30, 3.32, 3.37, 3.38), are linear functions of the constants C_i , which are, in turn, linear functions of grid temperatures, the thermal fluxes $\Delta\Phi_{i,j,h}^{HBS}$ and $\Delta\Phi_{i,j,e}^{XBS}$ can be considered as linear functions of grid temperatures too. On the other hand, the fluxes $\Delta\Phi_{i,j,e}^{EBS}$ exchanged through EBS elementary surfaces can be easily expressed in the same way by means of FVM. For this reason, all the previously considered quantities can be expressed as functions of the unknown grid temperatures. The iterative procedure chosen for solving this system of equations will be considered in the next section.

3.4.4 Iterative resolution procedure

The discretized equations for the fluid, given by Eq. (3.11), and for the wall, given by Eq. (3.18), have been expressed in terms of scalar variables. In order to adopt a matrix notation, the unknown fluid temperatures can be rearranged into the vector \mathbf{T}_f , the upstream temperatures into the vector \mathbf{T}_u and the unknown wall temperatures into the vector \mathbf{T}_w . As previously discussed, the fluxes exchanged through elementary surfaces ($\Delta\Phi_{i,j,e}^{EBS}$, $\Delta\Phi_{i,j,e}^{XBS}$ and $\Delta\Phi_{i,j,h}^{HBS}$) can be expressed as functions of the introduced vectors.

If the wall temperature profiles are somehow assumed, i.e. if the vector \mathbf{T}_w is known, then Eqs. (3.11) for the fluid define a closed linear system for the unknown

vector \mathbf{T}_f . The previous system of equations works like an operator FB , which allows us to update the temperature field inside fluid streams for given temperature profiles in the wall and given fluid inlet conditions, i.e. $FB(\mathbf{T}_w, \mathbf{T}_u) = \mathbf{T}_f$. It is possible to proceed in a similar way for the wall. Equations (3.15) allow us to explicitly calculate the thermal fluxes through the fin roots as functions of the unknown grid temperatures. If these fluxes are introduced in Eqs. (3.14), then a linear system of equations for the wall domain is obtained. If the fluid temperature profiles are somehow assumed, i.e. if the vector \mathbf{T}_f is known, then Eqs. (3.14, 3.15) for the wall define a closed linear system for the unknown vector \mathbf{T}_w . The previous system of equations works like an operator WB , which allows us to update the temperature field inside the wall for given temperature profiles of the fluid and given fluid inlet conditions, i.e. $WB(\mathbf{T}_f, \mathbf{T}_u) = \mathbf{T}_w$.

Hence the skeleton of the SEWTLE technique will be the following:

$$\text{Step 1} \quad \check{\mathbf{T}}_f = FB(\tilde{\mathbf{T}}_w, \mathbf{T}_u), \quad (3.39)$$

$$\text{Step 2} \quad \check{\mathbf{T}}_w = WB(\check{\mathbf{T}}_f, \mathbf{T}_u), \quad (3.40)$$

$$\text{Step 3} \quad \left| \frac{\Phi_H(\check{\mathbf{T}}_f, \tilde{\mathbf{T}}_w) - \Phi_C(\check{\mathbf{T}}_f, \tilde{\mathbf{T}}_w)}{\Phi_H(\check{\mathbf{T}}_f, \tilde{\mathbf{T}}_w)} \right| \leq Toll. , \quad (3.41)$$

where $Toll.$ is a given tolerance. The notation $\tilde{\mathbf{T}}$ indicates the values at the previous iteration, while $\check{\mathbf{T}}$ are the new values. Φ_H and Φ_C are respectively the hot-side and cold-side approximations of exchanged thermal power. As previously discussed, the final step requires the adopted numerical schemes to be intrinsically conservative.

At a generic step, for the resolution of the wall temperature field, an iterative procedure can be adopted for large heat exchangers: the simple Gauss-Seidel procedure is suggested. Since EBS is composed by surfaces linked together by transverse fins (see Figs. 3.2a, 3.2b), the Gauss-Seidel surface-by-surface method appears as

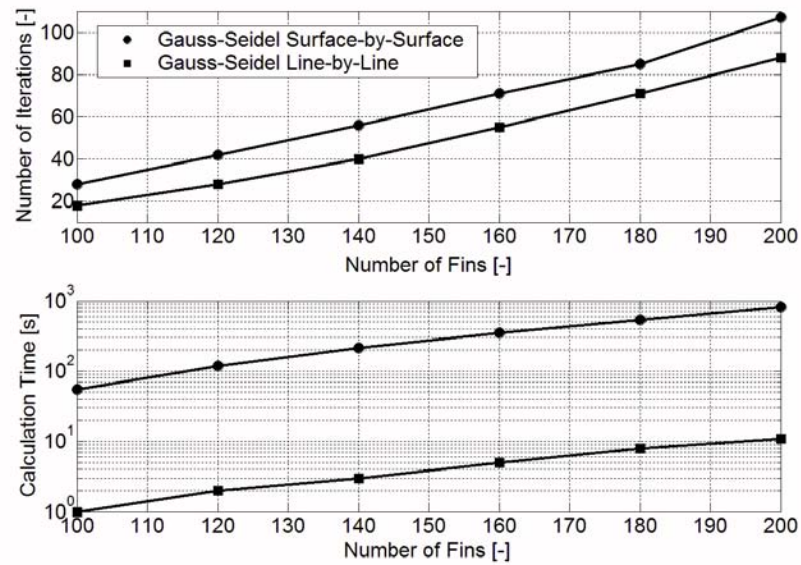


Figure 3.5: Comparison between GSSS (Gauss-Seidel surface-by-surface) and GSL (Gauss-Seidel line-by-line) method within a SEWTLE technique with control tolerance of 0.1 % on thermal power for a compact heat exchanger with mini/micro channels.

the most natural choice. In some cases, the resolution system for the generic EBS surface is large enough to suggest a further reduction by adopting the Gauss-Seidel line-by-line method which divides each surface into strips. In Fig. 3.5 a comparison between the Gauss-Seidel based methods is reported for a compact heat exchanger with mini/micro channels. When a fully three-dimensional description is needed, the Gauss-Seidel line-by-line method is preferable because it drastically reduces the computational time required by SEWTLE without increasing the number of iterations, which are very demanding if thermophysical properties depend on temperature.

3.5 Reliability check of numerical results

Some numerical results obtained with the developed numerical scheme and the consequent numerical code are reported for illustrating the advantages of the proposed methodology.

Table 3.1: Geometric parameters and operating conditions for the considered applications.

	Geometric parameters		Operating conditions	
Application 1				
	Fin length [mm]	16.0	Temp. top root [K]	390
	Fin height [mm]	3.2-9.0	Temp. bottom root [K]	340
	Fin thickness [mm]	0.1	Temp. fluid inlet [K]	300
			Temp. rise [K]	0-33
			Conductivity [W/mK]	200
Application 2				
	Plate length [mm]	250.0	Mass flow CO_2 [g/s]	43.0
	Plate width [mm]	16.5	Temp. inlet CO_2 [K]	351.4
	Plate height [mm]	1.65	Pressure CO_2 [bar]	76.6
	Channel number	11	Mass flow H_2O [g/s]	181.1
	Channel diam. [mm]	0.79	Temp. inlet H_2O [K]	300.0
	Fin height [mm]	8.8	Conductivity [W/mK]	200
	Fin thickness [mm]	0.1		
	Num. of plates	12		
	Num. of passes	3		
	Plates in 1th pass	5		
	Plates in 2nd pass	4		
	Plates in 3rd pass	3		

3.5.1 Model problems

Let us consider a thin plane which transfers heat to a surrounding fluid by convection and which is held at fixed temperature at the opposing bases. The temperature profile of the surrounding fluid depends on its specific heat capacity and mass flow rate: for simplicity, a linear temperature profile has been assumed.

The geometric parameters and the operating conditions are reported in Tab. 3.1. This problem is suitable to analyze the performances of a single smooth fin, according to classical theory of extended surface heat transfer [56]. The governing Eqs. (3.23) have been numerically solved by means of FEM with surrounded triangular elements. The discretization has been refined in order to produce a mesh independent solution,

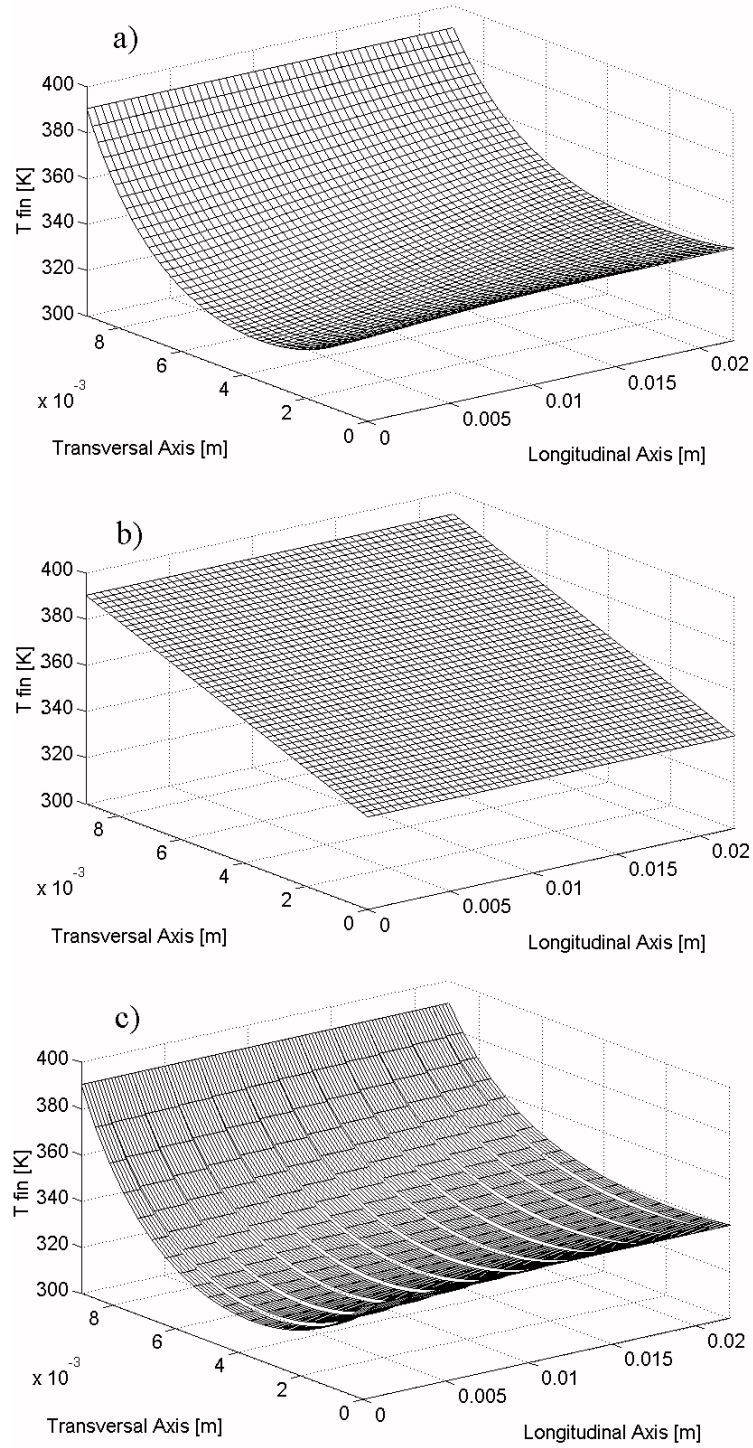


Figure 3.6: Fin temperature profiles described by different models: (a) high resolution FEM assumed as reference; (b) FVM description based on temperatures at fin roots and (c) intrinsically conservative FEM based on temperatures at fin roots.

Table 3.2: Results of calculations for single fin. The linear temperature profile has been assumed for fluid and the global temperature rise is $\Delta T_f = 0.0 K$.

z_0 [mm]	α [W/m ² K]	Bi	Thermal Power (W)			r	$(P - Q) / Q \times 100$	
			(Q) Ref.	Model FVM	(P) FEM		FVM	FEM
9.0	50	0.41	0.623	0.644	0.623	2.529	+3.37	+0.00
9.0	500	4.05	4.890	6.435	4.887	0.829	+31.60	-0.06
9.0	1000	8.10	8.060	12.870	8.051	0.743	+59.68	-0.11
9.0	1500	12.15	10.433	19.305	10.418	0.717	+85.04	-0.14
9.0	2000	16.20	12.364	25.740	12.341	0.707	+108.19	-0.19
8.4	2000	14.11	12.222	24.024	12.206	0.711	+96.56	-0.13
7.1	2000	10.08	11.781	20.306	11.764	0.727	+72.36	-0.14
5.4	2000	5.83	10.696	15.444	10.692	0.775	+44.39	-0.04
3.2	2000	2.05	7.858	9.152	7.855	1.010	+16.47	-0.04

which can be considered a reference for following comparisons (see Fig. 3.6a). Since the number of fins in a practical heat exchanger can be very high, a reduction of mesh density is needed. The simplest choice is to calculate convective thermal power by a linear temperature profile and then to subdivide it equally between fin roots (see Fig. 3.6b). The proposed methodology employs a shape function for temperature which takes into account the analytical solution of governing equations (see Fig. 3.6c). This strategy improves the accuracy in the calculation of convective heat transfer and allows us to properly estimate thermal fluxes at fin roots.

For the discussion of numerical results, some simplified analytical solutions can be useful. Let us suppose that $\alpha_{E,2s} = \alpha_{W,2s} = \alpha$ and $T_{f,E,2s} = T_{f,W,2s} = T_f(x)$. If the temperature rise for surrounding fluid can be neglected because of the high specific heat capacity, the model problem is highly simplified and the following solution yields:

$$\theta(z) = \frac{\theta_1 - \theta_2 a}{1 - a^2} \exp\left(\sqrt{Bi} \frac{z}{z_0}\right) + \frac{\theta_2 a - \theta_1 a^2}{1 - a^2} \exp\left(-\sqrt{Bi} \frac{z}{z_0}\right), \quad (3.42)$$

Table 3.3: Results of calculations for single fin. The linear temperature profile has been assumed for fluid and the global temperature rise is $\Delta T_f = 16.5 K$.

z_0 [mm]	α [W/m ² K]	Bi	Thermal Power (W)			r	$(P - Q)/Q \times 100$	
			(Q) Ref.	Model (P) FVM	FEM		FVM	FEM
9.0	50	0.41	0.544	0.562	0.544	2.824	+3.31	+0.00
9.0	500	4.05	4.274	5.618	4.267	0.877	+31.45	-0.16
9.0	1000	8.10	7.045	11.237	7.029	0.778	+59.50	-0.23
9.0	1500	12.15	9.121	16.855	9.096	0.749	+84.79	-0.27
9.0	2000	16.20	10.811	22.473	10.775	0.737	+107.87	-0.33
8.4	2000	14.11	10.676	20.975	10.657	0.742	+96.47	-0.18
7.1	2000	10.08	10.298	17.729	10.271	0.760	+72.16	-0.26
5.4	2000	5.83	9.359	13.484	9.335	0.815	+44.08	-0.26
3.2	2000	2.05	6.866	7.990	6.858	1.084	+16.37	-0.12

Table 3.4: Results of calculations for single fin. The linear temperature profile has been assumed for fluid and the global temperature rise is $\Delta T_f = 33.0 K$.

z_0 [mm]	α [W/m ² K]	Bi	Thermal Power (W)			r	$(P - Q)/Q \times 100$	
			(Q) Ref.	Model (P) FVM	FEM		FVM	FEM
9.0	50	0.41	0.465	0.480	0.465	3.219	+3.23	+0.00
9.0	500	4.05	3.657	4.802	3.647	0.941	+31.31	-0.27
9.0	1000	8.10	6.030	9.603	6.008	0.825	+59.25	-0.37
9.0	1500	12.15	7.809	14.405	7.774	0.791	+84.47	-0.45
9.0	2000	16.20	9.258	19.206	9.209	0.777	+107.45	-0.53
8.4	2000	14.11	9.117	17.926	9.108	0.783	+96.62	-0.10
7.1	2000	10.08	8.816	15.151	8.778	0.805	+71.86	-0.43
5.4	2000	5.83	8.011	11.524	7.978	0.869	+43.85	-0.41
3.2	2000	2.05	5.875	6.829	5.861	1.183	+16.24	-0.24

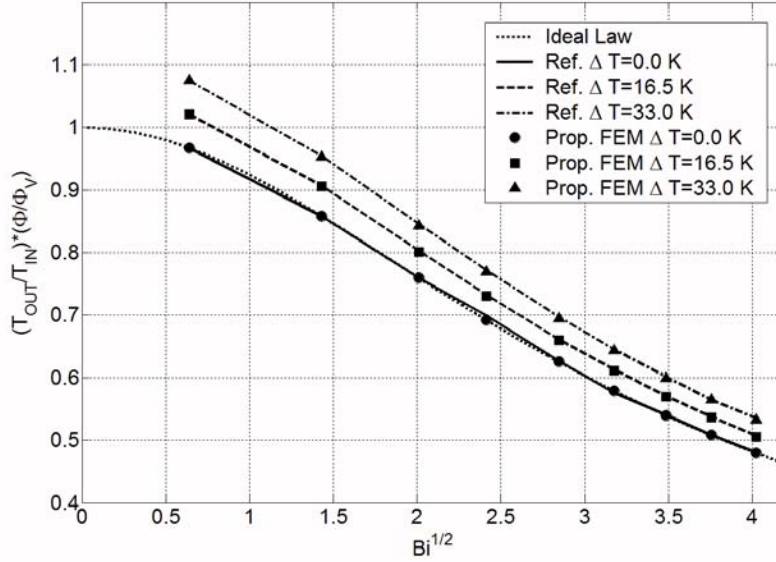


Figure 3.7: Results of calculations for single fin. The thermal powers calculated by the proposed methodology and the reference are reported for different temperature rises of the fluid. The ratio T_{OUT}/T_{IN} helps to distinguish the results of simulations.

where

$$\theta(z) = T_w(z) - T_f,$$

$$\theta_1 = T_w(0) - T_f,$$

$$\theta_2 = T_w(z_0) - T_f,$$

$$Bi = 2 \frac{\alpha z_0^2}{\lambda_w s}, \quad a = \exp \sqrt{Bi}.$$

The ratio between the convective thermal power calculated with the exact temperature profile and that obtained with a linear profile can be expressed in the following way:

$$\left(\frac{\Phi}{\Phi_V} \right)_{\Delta T_f=0} = \frac{\int_0^{z_0} \int_0^{x_0} \alpha (T_w - T_f) dx dz}{\int_0^{z_0} \int_0^{x_0} \alpha (T_w^V - T_f) dx dz} = \frac{2}{\sqrt{Bi}} \frac{\exp \sqrt{Bi} - 1}{\exp \sqrt{Bi} + 1} < 1. \quad (3.43)$$

This ratio has been labeled as ideal law in Fig. 3.7. The linear temperature profile adopted by FVM can be considered a good approximation at small Biot numbers.

Otherwise the convective heat transfer forces to consider more complex shape functions. Tabs. 3.2, 3.3, 3.4 report the results of some numerical simulations performed by varying Biot number and temperature rise for the surrounding fluid. The effect of temperature rise, which determines the longitudinal conduction, increases the characteristic ratio if compared with the ideal law, namely

$$\left(\frac{\Phi}{\Phi_V} \right)_{\Delta T_f=0} < \frac{\Phi}{\Phi_V} < 1. \quad (3.44)$$

Three simulations are shown in Fig. 3.7. In all cases, the proposed conservative element reproduces very well the reference ($\Phi_E \approx \Phi$) and reveals its superiority at high Biot number in comparison with finite volume description involving the same number of nodes ($\Phi_V > \Phi$).

The accuracy is not the only aspect to be considered. The thermal balance of the generic fin can be expressed by the splitting factor r , defined as

$$r = \frac{\int_0^{x_0} \lambda_w \left[\frac{\partial \theta(x,z)}{\partial z} \right]_{z=z_0} s dx}{\int_0^{z_0} \int_0^{x_0} \alpha (T_w - T_f) dx dz}, \quad (3.45)$$

and its complement r^* , which is defined such as $r + r^* = 1$. When $r < 0$ or $r > 1$, a thermal short circuit exists, i.e. one of fin roots is characterized by inverse thermal flux directed towards the heated wall. Tabs. 3.2, 3.3, 3.4 report the splitting factor calculated by the proposed conservative FEM. Since FVM subdivides equally the convective thermal power between fin roots, it is characterized by a fixed value of splitting factor $r = r^* = 1/2$. On the other hand, the proposed conservative element enables us to calculate the real distribution of thermal fluxes at any Biot number. The adopted boundary conditions for proposed element guarantee the continuity of thermal power, which can be employed as a convergence check into the SEWTLE technique.

The description of fins constitutes an essential step for analyzing the performances

Table 3.5: Results of calculations about mini/micro channel heat exchanger.

N. fins		Fin model / Divider model				$(P - Q)/Q \times 100$
		$V/V(P)$	V/E	E/V	$E/E(Q)$	
110	N. iter.	317	317	335	330	-3.94
	Time (s)	30	32	34	34	-11.76
	Power (W)	2402	2402	2305	2305	+4.21
220	N. iter.	292	293	318	318	-8.18
	Time (s)	54	57	62	66	-18.18
	Power (W)	2624	2624	2469	2469	+6.28
330	N. iter.	282	277	313	310	-9.03
	Time (s)	76	79	90	95	-20.00
	Power (W)	2791	2790	2604	2604	+7.18
440	N. iter.	273	272	318	311	-12.22
	Time (s)	96	101	119	122	-21.31
	Power (W)	2923	2923	2717	2717	+7.58
550	N. iter.	277	274	325	319	-13.17
	Time (s)	119	125	151	155	-23.23
	Power (W)	3033	3033	2812	2812	+7.86
660	N. iter.	287	280	336	332	-13.55
	Time (s)	149	150	185	189	-21.16
	Power (W)	3123	3123	2897	2896	+7.84
770	N. iter.	299	292	351	346	-13.58
	Time (s)	175	181	223	230	-23.91
	Power (W)	3200	3200	2971	2971	+7.71
880	N. iter.	313	306	376	366	-14.48
	Time (s)	208	214	270	277	-24.91
	Power (W)	3266	3266	3037	3037	+7.54

of the whole heat exchanger. If a single fin is considered, there is no need to employ numerical schemes which are intrinsically conservative because only a local convergence criterion must be satisfied. On the other hand, the heat exchanger analysis needs some iteration procedure and a global convergence criterion. Since the SEW-TLE technique uses the transferred thermal power as a convergence criterion, no lack of continuity for this quantity can be accepted in the discretized equations. As pre-

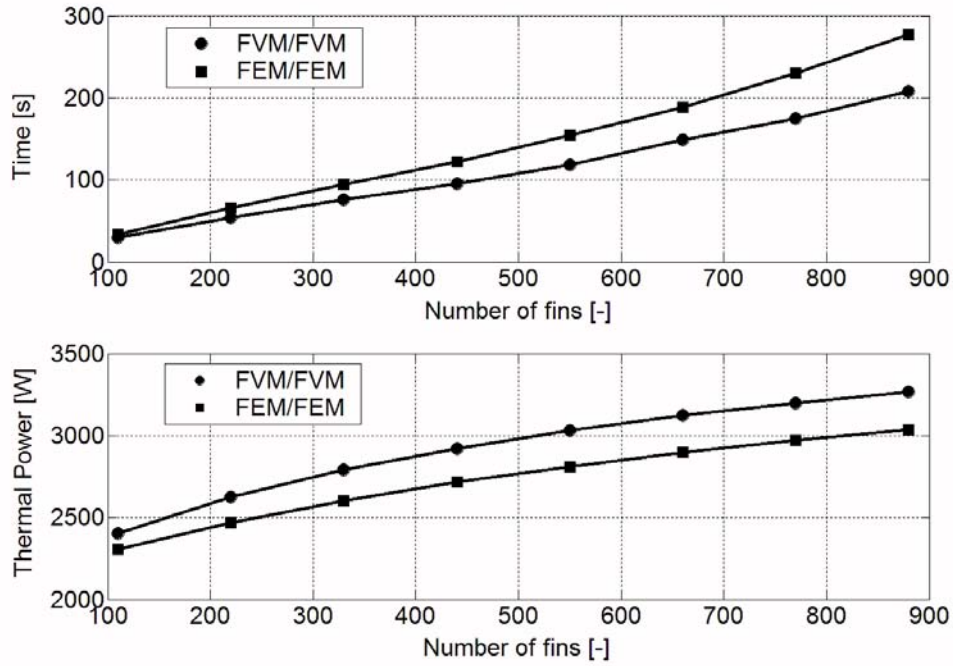


Figure 3.8: Results of calculations about mini/micro channel heat exchanger. Since the fin temperature profiles due to FVM with the adopted meshes are inaccurate, it is possible to conclude that FVM requires less calculation time but underestimates the exchanged thermal power.

viously discussed, the proposed conservative elements satisfy this condition because they exactly ensure thermal balance ($r + r^* = 1$), while the surrounded elements do it only asymptotically ($r + r^* \rightarrow 1$).

A numerical code has been developed from scratch for obtaining a fully-three dimensional description of cross-flow multi stream compact heat exchangers. The fins can be described either by FVM or FEM with a proposed conservative element in order to investigate the most suitable technique and its effect on computational time. As a preliminary example, let us consider a mini/micro channel heat exchanger which cools a given mass flow rate of carbon dioxide by means of a water flow. The geometric parameters and the operating conditions are reported in Tab. 3.5. The mini/micro channels, in which carbon dioxide flows, are identified by vertical separating walls,

called dividers, which represent a special kind of extended surfaces (see Fig. 3.2*b*). Table 3.5 reports the results of some numerical simulations performed by varying the numerical scheme for the extended surfaces and the number of fins. The effect of the numerical scheme depends on the Biot number of the considered surface. Since the Biot number for fins is quite high ($Bi = 7.7$) while the one for dividers is negligible ($Bi = 0.1$), the calculated thermal power is mainly affected by the numerical scheme selected to describe fins. For low numbers of fins ($N = 110 - 550$), an increase of water-side extended surface increases the relative discrepancy between FVM and proposed FEM (4.2–7.9 %). For high numbers of fins ($N = 550 - 880$), an additional increase reduces the relative discrepancy (7.9–7.5 %) because the heat exchanger performances are less influenced by the heat transfer surface. All the simulations show that the proposed FEM requires a greater computational time than FVM with the same number of grid nodes because the exponential function must be evaluated. However the FVM requires much finer meshes, if the same accuracy for calculating the thermal fluxes at fin roots is desired. However, since the number of grid nodes required by FVM in order to produce the same accuracy due to analytical solutions of the conduction equation in fins is huge, the increase in the computational time for calculating the exponential functions can be considered a modest drawback.

In Fig. 3.8, the computational time and the calculated thermal power for selected methods are reported. This second application shows that the proposed FEM should be considered to model every portion of extended surface characterized by high Biot numbers, even though this requires additional computational efforts.

3.5.2 Comparison with experimental data

In order to verify the reliability of the numerical code, a comparison between simulation results and experimental data was carried out. The experimental data

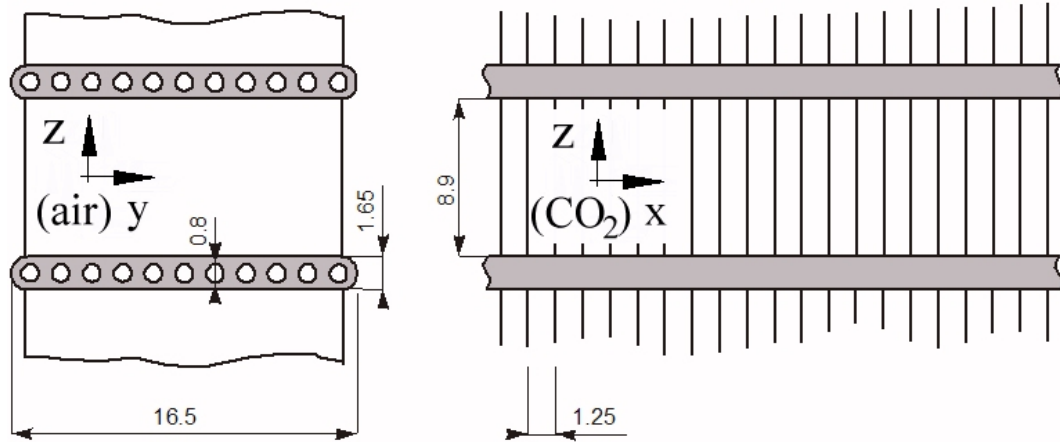


Figure 3.9: Basic geometry of the considered mini/micro channel compact heat exchanger. The frontal area is equal to $545 \times 350(z)$ mm. The number of flat tubes is equal to 34 and they are subdivided into 3 passages [57].

were found in literature [57] and cover a wide range of operating conditions of a current gascooler for automotive applications, which realizes carbon dioxide cooling by means of under-hood air. The most relevant sizes of the considered device are reported in Fig. 3.9. This typical heat exchanger is composed of a single array of flat tubes in which circular mini/micro channels exist where carbon dioxide flows. Two cylindrical headers are connected at the opposite ends of the tube array for feeding and discharging the refrigerant; the headers can be interrupted at different level so as to force the flow to have more passes inside the heat exchanger (two interruptions and three passes occur in the case considered in this work, as shown in the following). Two adjacent flat tubes are linked together by an array of fins that are brazed on the flat surfaces of the tubes and form the channels in which air moves in cross-flow with respect to refrigerant. The air streams along the y -axis while the carbon dioxide streams along the x -axis.

Some phenomenological correlations have been included in the numerical code in order to characterize pressure drop and convective heat transfer for both the fluids,

i.e. air and carbon dioxide. The pressure drops can be divided in two categories, the localized ones due to inflow and outflow fluid sections and the distributed ones spread along the fluid stream. In this case we are interested in the thermal efficiency of these devices and for this reason the carbon dioxide pressure drops are most relevant because they could indirectly affect the heat transfer. The phenomenological correlations of Chang and Wang [58] and that of Idelchik [59] have been used for predicting the localized and the distributed air pressure drops respectively. Moreover, the phenomenological correlations of Churchill [60] and again that of Idelchik [59] have been used for predicting the localized and the distributed carbon dioxide pressure drops respectively. On the other hand, the phenomenological correlations for predicting convective heat transfer coefficients are quite accurate for air and a recent correlation due to Chang and Wang has been used [61]. Unfortunately the situation is not so clear for carbon dioxide cooling close to the critical point. In this case, many phenomenological correlations exist, although their predictions show relevant discrepancies. In the next chapter, this problem will be extensively discussed. Here the main conclusion is disclosed in advance and the phenomenological correlation of Pettersen et al. [62] will be adopted.

The simulation speed and the results accuracy depend on the number of grid nodes in the section of the mini/micro channel tube; the best definition is the one that considers the number of virtual mini/micro channels equal to the real case, but a smaller number can be chosen for simplifying the calculation. Essentially this defines the mesh grid refinement used in the reported calculations.

In Fig. 3.10, the calculated values of the total heat transfer rate are reported against the experimental values; the simulation slightly overestimate the real thermal performance, but the accuracy is high, since most of the errors are smaller than

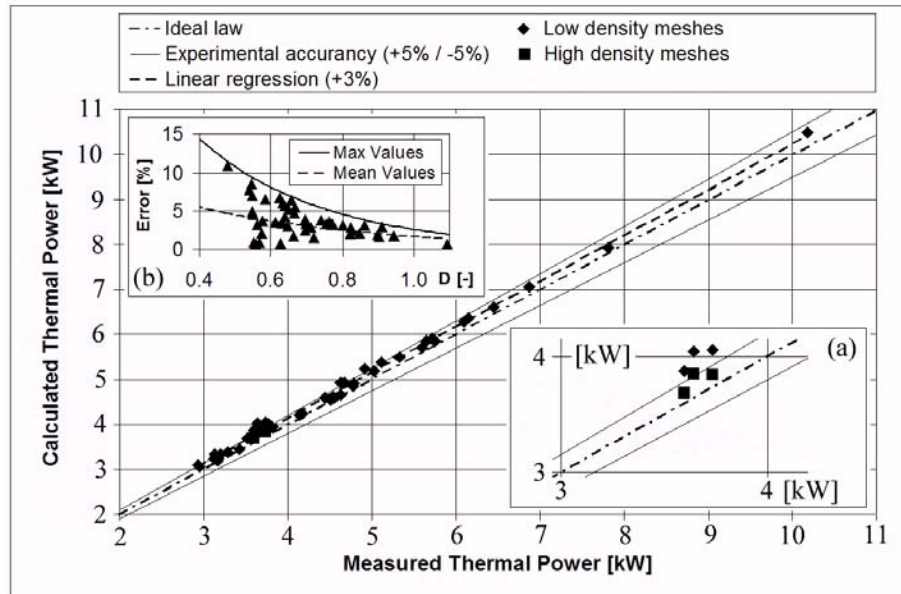


Figure 3.10: Comparison between total heat flow calculated by the numerical code and experimental data [57]. (a) Simulations performed with detailed meshes: run #9, #32 and #37. (b) Correlation between error and factor D accounting for operation near the critical point.

3%, being the maximum error around 6%. The Fig. 3.10a reports the improvement in numerical accuracy of three critical cases, obtained by considering high-density meshes. Even though from these results the simulation model appears reliable and accurate, it is worth noting that this high accuracy could be related to the high thermal efficiency of the gascooler, that makes thermal power not very sensitive to heat transfer characteristics. Essentially, the heat exchanger appears grossly over-sized. Furthermore, the total heat flow exchanged is strongly dependent on the correlations chosen to evaluate the heat transfer coefficients. On the other hand, applying the direct numerical analysis of convective heat transfer has been considered impractical, because it would have required a tremendous increase in the mesh size.

It is interesting to investigate the effect of the mesh resolution on the final results, since in transcritical CO_2 cycles the modeling of the cooling process at high pressure

Table 3.6: Effects of mesh resolution on heat flow. Run #9: carbon dioxide mass flow rate 31.49 g/s, carbon dioxide inlet temperature 66.50 °C and inlet pressure 88.58 bar; air mass flow rate 452.0 g/s and air inlet temperature 31.8 °C [57].

Run	Virtual mini/micro channels	Heat flow					Error (2)/(1) [%]
		Measured (1) [W]	Code (2) [W]	I [W]	II [W]	III [W]	
#9	1	3643	4041	2418	1027	595	+10.9
#9	3	3643	3887	2354	976	557	+6.7
#9	5	3643	3872	2324	975	572	+6.3
#9	7	3643	3820	2250	975	595	+4.9
#9	9	3643	3836	2251	978	607	+5.3
#9	11	3643	3845	2251	987	607	+5.5

raises some problems related to transformation close to the critical point, where very large variations of the thermodynamical and thermophysical properties occur.

To this end, a dimensionless parameter, $D = \sqrt{[p_{in}/p_{cr} - 1]^2 + [h_{in}/h_{cr} - 1]^2}$, was proposed to quantify the proximity of the inlet operating conditions (p_{in} , h_{in}) to the critical point (p_{cr} , h_{cr}). This parameter can help to discuss the distribution of error $E = |\Phi - \Phi_{exp}|/\Phi_{exp}$, where Φ is the heat flow predicted by the numerical code and Φ_{exp} is the experimental heat flow. Although the error distribution is quite scattered, as shown in Fig. 3.10b, the trend curve can be described with reasonable accuracy by the following equation, which clearly demonstrates that errors increase when the system is operating near the critical point:

$$E = E_0 \exp(D/D_0), \quad (3.46)$$

where E_0 and D_0 are factors that defines the error trend curve (the lower one in Fig. 3.10b).

To analyze the sensitivity of the simulation errors to the mesh resolution, the calculation for run #9 [57], which is a critical case for the operating conditions, was

Table 3.7: Effects of pressure drops on heat flow. The results due to the original phenomenological correlation have been multiplied by a proper factor for realizing artificially increased pressure drops. Run #9: carbon dioxide mass flow rate 31.49 g/s, carbon dioxide inlet temperature 66.50 °C and inlet pressure 88.58 bar; air mass flow rate 452.0 g/s and air inlet temperature 31.8 °C [57].

Run	Pressure drop factor	Heat flow		
		Measured (1) [W]	Code (2) [W]	Error (2)/(1) [%]
#9	1	3643	4041	+10.9
#9	2	3643	4022	+10.4
#9	3	3643	4002	+9.9
#9	4	3643	3983	+9.3

repeated, increasing the number of nodes from the most simplified case. Increasing the number of nodes in the cross section perpendicular to the flow of carbon dioxide brings about a better accuracy in representing the thermal fields in the system. From a physical point of view, this is equivalent to increasing the number of virtual mini/micro channels inside the flat tube. When the number of virtual mini/micro channels is equal to the real number of mini/micro channels in the gascooler, the maximum possible accuracy is reached. The results of this comparison are shown in Tab. 3.6; we note that increasing the number of virtual channels from 1 to 3 greatly improves the accuracy in evaluating heat flow, but a further increase in the mesh resolution does not produce a significant benefit. In the same Tab. 3.6 the total heat flow was subdivided into three contributions, referring to the three heat exchanger sections, corresponding to the three gas passages; the deviations of the calculated values for different numbers of virtual channels with respect to the most simplified case (one virtual channel) can give an account of the effect of the mesh size on the heat transfer prediction for heat exchangers of different effectiveness, or subject to different heat flow: as expected, when comparing the deviations for passage I and

for the whole heat exchanger, high heat flux calls for high resolution, because the consequent high temperature gradients require more detail in describing the process.

As far as the refrigerant pressure drop is concerned, in some papers [63] it is asserted that most of the traditional correlations underestimate the experimental data: this has been confirmed by the results of the simulations, which show an average mean error of -70% in predicting pressure drop. This error matches previous conclusions on the same subject [57, 63]. To investigate the effect of this variable on heat flow, simulations have been carried out having increased, according to different arbitrary multiplying factors, the values of pressure drop calculated from the correlations previously discussed. The results in Tab. 3.7 demonstrate that the influence of pressure drop on the overall heat transfer performance is negligible in the case here considered and seem to confirm the underestimation deriving from current correlations.

3.6 Undesired effects due to thermal conduction

The accurate numerical model previously discussed has been developed for analyzing the possible drawbacks of the common assumptions used to simplify the solution of the equations related to conduction inside metal for compact heat exchangers involved in the carbon dioxide cooling of transcritical cycles. The numerical code takes into account the real distribution of heat flux due to transverse and longitudinal conduction along both tubes and fins. In the following sections, the numerical results will be discussed.

3.6.1 Thermal conduction in fins

The numerical code described in the previous sections can be used to investigate some phenomena usually neglected in evaluating the fins efficiency. In modeling

compact heat exchangers, a usual approximation is used, consisting in the half-fin-length idealization. According to this idealization, the fin section at the middle distance from the tubes is assumed as adiabatic; this is strictly true only when the fin bases are both at the same temperature. In a real case, these temperatures in general are different and, as a consequence, the adiabatic line is shifted from the middle position, so that the two heat transfer pathways do not have the same length. In extreme cases, the adiabatic line is not present on the fin and the two tubes are subject to opposite heat flows (entering one tube and exiting from the other). The last case identifies a thermal short circuit.

The transverse heat flows for unit length q_1 and q_2 at fin roots 1 and 2 can be expressed by the following correlations, respectively [56]:

$$q_1(y) = \frac{s \omega \lambda_w}{\sinh(\omega z_0)} [\theta_1 \cosh(\omega z_0) - \theta_2] = q_1^*(y) - \frac{s \omega \lambda_w}{\sinh(\omega z_0)} (\theta_2 - \theta_1), \quad (3.47)$$

$$q_2(y) = \frac{s \omega \lambda_w}{\sinh(\omega z_0)} [\theta_2 \cosh(\omega z_0) - \theta_1] = q_2^*(y) + \frac{s \omega \lambda_w}{\sinh(\omega z_0)} (\theta_2 - \theta_1). \quad (3.48)$$

where q_2^* and q_1^* are the heat flows per unit length predicted by the half-fin-length idealization. To discuss the adequacy of this idealization, it is useful to consider the splitting factor r , previously defined by Eq. (3.45). This can be reformulated by means of the root heat flows per unit length:

$$r = \frac{\int q_2(y) dy}{\int [q_2(y) + q_1(y)] dy}, \quad (3.49)$$

where the heat flow due to thermal conduction is considered positive if entering the fin. The previous integrals are applied to the whole fin length, which coincides with the length of the air stream. The half-fin-length idealization is exactly complying with reality when the temperature differences at both ends are equal, i.e. $\theta_1 = \theta_2$; in this case the splitting factor is $r = 1/2$. For most of the typical operating conditions of multi-stream plate fin heat exchangers, this condition is very close to be fulfilled

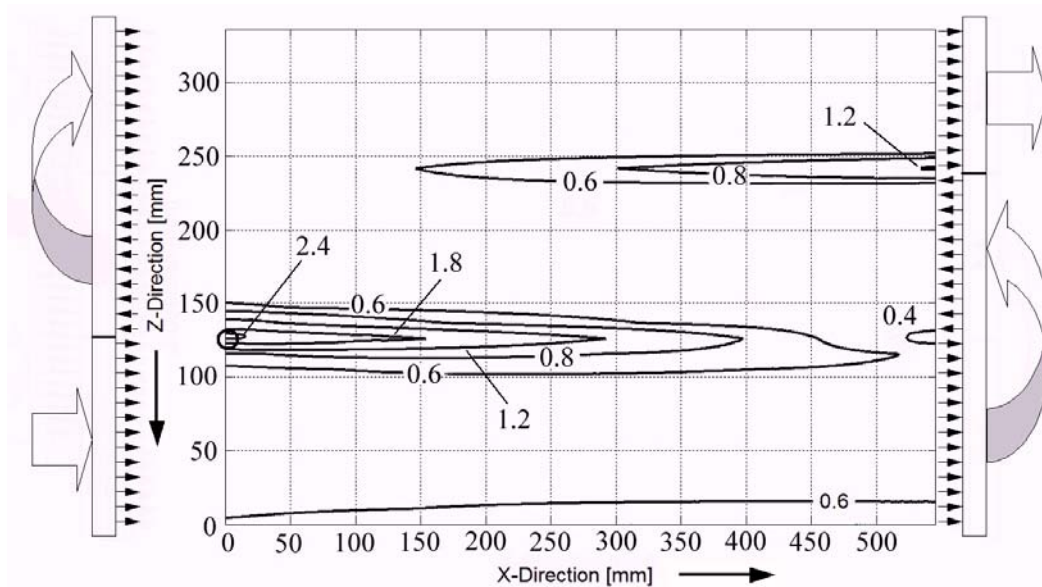


Figure 3.11: Contour lines of the splitting factor for conductive heat flow at fin roots (air side frontal view, XZ plane in Fig. 3.9).

and the half-fin-length approximation produces acceptable errors. When θ_2 greatly differs from θ_1 , the splitting factor is far from $1/2$ and therefore, in these cases, the half-fin-length idealization is not acceptable any longer.

Another widely employed approximation in modeling heat transfer with extended surfaces suggests to neglect the thermal conduction along the air flow direction. For louvered fins, the longitudinal conduction must take into account the effect of the interruptions by a suitable value of equivalent directional thermal conductivity. To verify the accuracy of the commonly used simplifying hypotheses, a detailed simulation was performed. In particular, run #32 [57] was considered: the mass flow rate of carbon dioxide was 26 g/s , the inlet pressure was 76 bar and the inlet temperature was $78.2 \text{ }^\circ\text{C}$, while for air the mass flow rate was 454 g/s and the inlet temperature was $26.8 \text{ }^\circ\text{C}$.

In Fig. 3.11 the contour lines of the splitting factor are reported for the heat

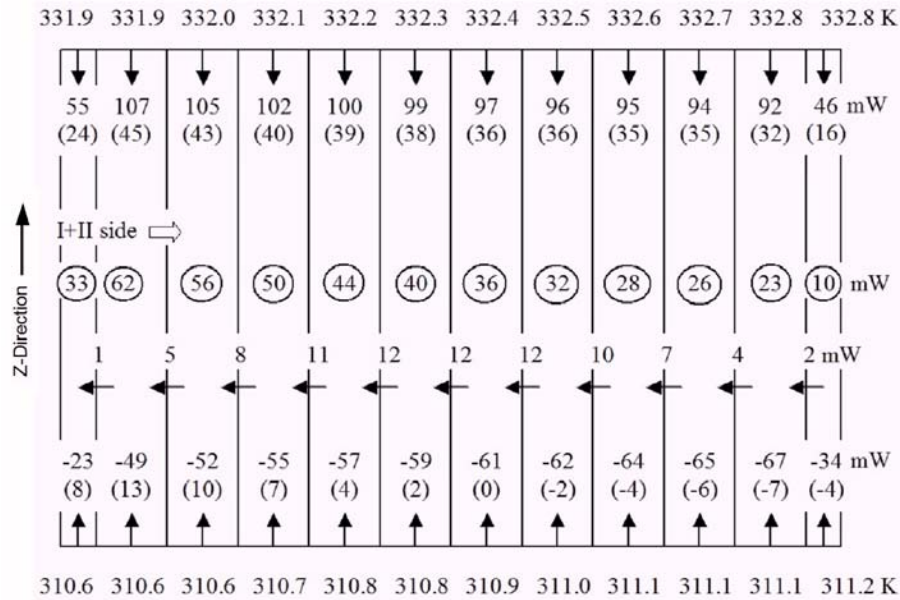


Figure 3.12: Thermal variables in a fin ($r = 2.47$) located between the first and the second passage (in the position marked with the circle in Fig. 3.11). Black arrows refer to conductive heat flows (transverse and longitudinal). Values inside circles refer to convective thermal fluxes. Values inside parentheses refer to half-fin-length idealization.

exchanger face area; this variable is not defined in all points of the face area, but only for fins and, consequently, the curves are built by linking points located on the fins; moreover, in the definition of the splitting factor, given by Eq. (3.49), subscript 2 refers to the fin root characterized by greater z coordinate (upper fin root). This means that for $r > 1/2$ a thermal short circuit exists from upper (2) to lower fin root (1).

Only few fins are characterized by splitting factors far from the ideally assumed value $r = 1/2$; they are located between flat tubes which are close to different refrigerant passages, where the temperature difference between the refrigerant flowing inside adjacent tubes is large. In this situation, the half-fin-length idealization introduces a significant error in estimating the thermal fluxes distribution and the related temperature field inside the metal. However since $q_1^* + q_2^* = q_1 + q_2$, as follows from

Table 3.8: Effects of different assumptions in fin modelling on heat flow prediction. Run #27, 32, 36: carbon dioxide mass flow rate 25.11, 26.04, 25.55 g/s , carbon dioxide inlet temperature 96.9, 78.2, 95.4 $^{\circ}C$ and inlet pressure 95.93, 76.59, 93.85 bar ; air mass flow rate 453.0, 454.0, 710.0 g/s and air inlet temperature 43.0, 26.8, 43.6 $^{\circ}C$ [57].

Run	Fin modeling	Heat flow		
		Measured (1) [W]	Code (2) [W]	Error (2)/(1) [%]
#27	Half-Fin-Length Idealization	3285	3420	+4.1
#27	Improved Temperature Field	3285	3385	+3.0
#32	Half-Fin-Length Idealization	3596	3918	+9.0
#32	Improved Temperature Field	3596	3879	+7.9
#36	Half-Fin-Length Idealization	3138	3353	+6.9
#36	Improved Temperature Field	3138	3327	+6.0

Eqs. (3.48, 3.49), it can be concluded that the half-fin-length idealization correctly predicts the total heat transfer from/to a fin, but not the individual heat flows at the roots. This involves a modest effect on the prediction of the total heat transfer rate, as results from Tab. 3.8.

In Fig. 3.12 some relevant values of the thermal fluxes are shown for a discretized fin, subdivided into vertical strips linking two adjacent tubes. According to a common practice, the shape function adopted to describe the temperature distribution inside each discretized portion of the fin has been previously described referring to the local coordinate system. Instead, in Fig. 3.12, all the discretized strips are reported at the same time in the plane identified by y-axis and z-axis, in order to analyze the mutual exchange of thermal power. The values inside the circles show the total convective heat flow exchanged with air on both fin sides. The values at the fin root show the heat flow entering (positive value) or exiting (negative values) from the fin; the values inside parentheses refer to heat flow predicted by the half-fin-length idealization. The temperatures at the fin roots are printed outside the fin contour. The longitudinal

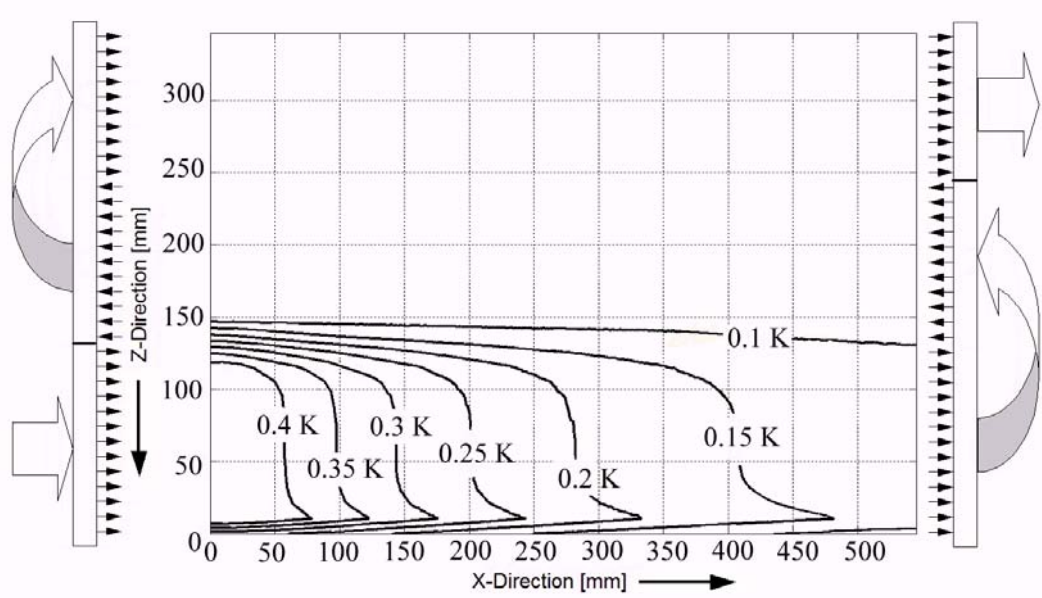


Figure 3.13: Contour lines of the temperature variance in the cross sections of flat tubes (air side frontal view, XZ plane in Fig. 3.9).

heat flow by conduction is indicated next the related arrows. For the considered fin, the splitting factor r is equal to 2.47, which is very close to the maximum value in Fig. 3.11, and entails a reversed conductive flux (i.e. from the fin to the tube) at the lower fin root. The sum of heat flow entering both the fin bases is equal to 440 mW , as predicted by the half-fin-length idealization, according to the theory. The longitudinal conductive heat flow along the air flow direction shows its maximum at the central portion of the fin, while it is very small at both fin ends; however the maximum value, which is equal to 12 mW , is nearly negligible if compared with the transverse conductive heat flow.

3.6.2 Thermal conduction in mini/micro channel tubes

It is common practice to consider the tube wall temperature on any cross section and to neglect the heat flowing longitudinally by conduction through the walls, even if longitudinal temperature gradients exist. Instead, the present simulation code takes

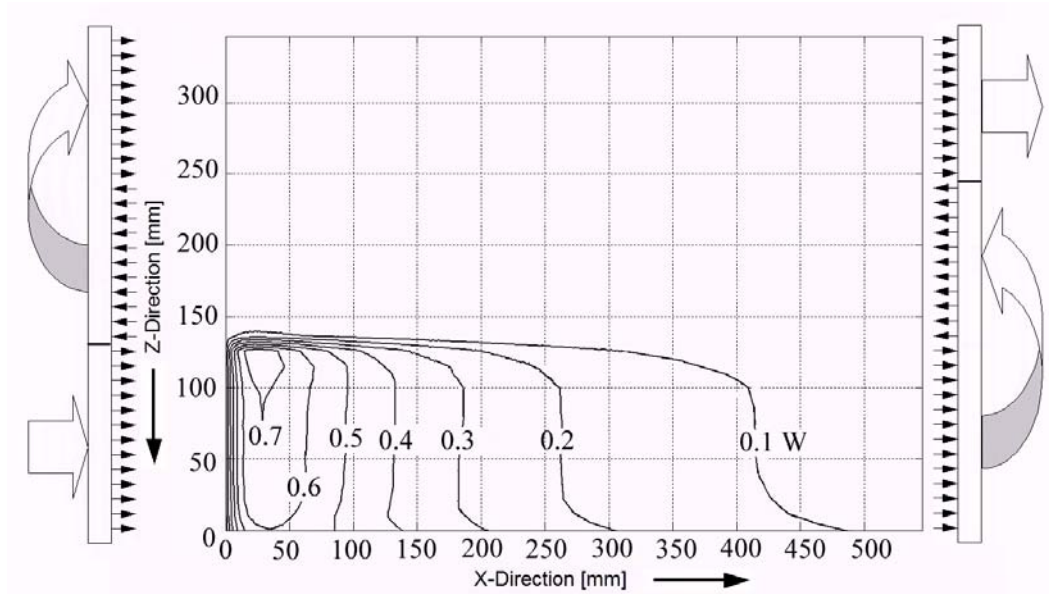


Figure 3.14: Contours lines of longitudinal conductive heat flow in flat tubes (air side frontal view, XZ plane in Fig. 3.9).

into account these heat transfer aspects and therefore can quantify the error associated with the mentioned simplifying assumptions. In the following Figs. 3.13 and 3.14, some of the numerical results are reported, referring to the operating conditions of run #32 [57], already considered in Fig. 3.11.

A factor ζ has been defined to take into account the non-uniformity of the temperature field in the cross section of the mini/micro channel tubes. If the cross section is subdivided into N elements:

$$\zeta = \sqrt{\sum_{n=1}^N A_n \left[T_n - \frac{\sum_{m=1}^N (A_m T_m)}{\sum_{m=1}^N A_m} \right]^2} / \sum_{n=1}^N A_n. \quad (3.50)$$

The contour lines of factor ζ for the cross sections of mini/micro channel tubes are plotted in Fig. 3.13. Despite the fact that ζ is meaningful only for the tube section, for the sake of readability, the curves are built by linking all points with equal ζ values (the same was done in Fig. 3.14 too).

According to the heat flux resulting from simulations, compared with the one of an

Table 3.9: Effects of conduction modeling on heat flow. Run #11, 32: carbon dioxide mass flow rate 22.08, 26.04 g/s , carbon dioxide inlet temperature 103.0, 78.2 $^{\circ}C$ and inlet pressure 105.55, 76.59 bar ; air mass flow rate 453.0, 454.0 g/s and air inlet temperature 32.4, 26.8 $^{\circ}C$ [57].

Run	Conduction modeling	Heat flow		
		Measured (1) [W]	Code (2) [W]	Error (2)/(1) [%]
#11	Reference	4774	4845	+1.5
#11	No Cond. Longitudinal Fin	-	4844	+1.5
#11	No Cond. Longitudinal Tube	-	4845	+1.5
#11	No Cond. Transverse Tube	-	4843	+1.4
#32	Reference	3596	3879	+7.9
#32	No Cond. Longitudinal Fin	-	3879	+7.9
#32	No Cond. Longitudinal Tube	-	3882	+8.0
#32	No Cond. Transverse Tube	-	3878	+7.8

ideal case with isothermal cross section, it follows that the common assumptions can be considered fully acceptable. This holds also for the most critical sections located at the inlet of refrigerant, where there is the maximum temperature difference between the fluids and, consequently, the maximum heat flux.

In Fig. 3.14 the contours lines of the longitudinal heat flow by conduction along the tube walls (along the direction of the refrigerant flow) are plotted. The numerical results of Fig. 3.14 show that the longitudinal heat flow can be neglected in describing the heat transfer process in such a kind of heat exchanger, even for the tubes subject to the maximum temperature gradients. In fact, the order of magnitude of the overall heat flow for a single tube is about 100 W .

To complete the analysis of the effect of the thermal conduction inside the metal, with reference to the simplifications assumed in the traditional numerical codes, other simulations have been performed, setting to zero, one at a time, the thermal conductivity along different directions, except the one orthogonal to the fin bases. From

the results, shown in Tab. 3.9, it can be inferred that the longitudinal conduction, both in fins and tubes, and the transverse conduction in tubes are not significant for the thermal process; hence it results that, even though the traditional calculation procedures do not take into account these effects, they do not produce any significant loss of accuracy.

3.7 Conclusions

In this section, an original numerical method has been developed for numerically investigating mini/micro channel compact heat exchangers in order to evaluate the effects due to undesired conduction. The developed numerical code considers the effects of axial conduction along the tube length, as well as conduction between adjacent tubes through the air-side fins attached to them. The various temperature gradients in each of these directions were analyzed to estimate the deterioration in performance that can be expected from these parasitic heat transfer processes.

Even though the adjacent tubes can be very close to each other in order to realize compact devices, the temperature difference between different passages can be relevant because of the supercritical cooling and the fact that these gascoolers are usually made of aluminum, which has high thermal conductivity, the numerical simulations suggest that the parasitic heat transfer processes are substantially negligible for the considered operating conditions. This result confirms that some of the prejudices against these compact heat exchangers, which limit their widespread diffusion in practice, are not completely justified.

It has been pointed out that the considered experimental data refer to a gascooler characterized by high thermal efficiency, which makes the thermal flux not very sensitive to the heat transfer characteristics. Essentially, the heat exchanger appears

grossly over-sized. These experimental data have been selected for validating the numerical results because, in this way, the numerical modeling is largely independent of the inaccuracies due to the phenomenological correlations used to estimate the convective heat transfer of carbon dioxide in mini/micro channels. Otherwise the numerical results would depend on both the implemented algorithm and the reliability of the considered phenomenological correlation. Since relevant discrepancies exist among different phenomenological correlations, the numerical results themselves would be inconclusive. In the next Chapter 4, this problem will be properly investigated.

